

Laser-controlled intermetallics synthesis during surface cladding

11

I.V. Shishkovsky^{1,2}

¹Lebedev Physics Institute (LPI) of Russian Academy of Sciences, Samara, Russia;

²Moscow State Technological University named "STANKIN", Moscow, Russia

11.1 Introduction

The selection of promissory powder compositions for laser cladding (LC) is traditionally based on the conditions of a metallurgical miscibility (the possibility to form a eutectic) first in the liquid and then in crystallizing phases after the laser treatment (LT). If the melting point of the cladding powder is lower than the substrate temperature, then a good wettability of the melt provides the required contact conditions. Otherwise, the intermixing of unfused cladding particles occurs in the melting pool of the substrate, and this is called the metal-matrix (MM), ceramic-matrix (CM) hardening after the crystallization. During the melting process, the fusible phase spreads by the grain boundaries of the refractory phase and, being crystallized, serves as a binder that reinforces the surface strength after the laser influence (LI). These hardened inclusions substantially improve the physical and mechanical properties by MM composites.

Hence, in parallel with the search for new challenging possibilities of powdered systems for LC and with the expansion of the synthesized parts of the functional resource, it seems reasonable to concurrently use functionally graded (FG) composite materials, as well as to use combinations of LC with other processes [1]. Thus, the combination of LC with soldering makes it possible to produce three-dimensional (3D) models out of bimetals having a high adhesion of the solder melt to the metallic phase, ensuring the improved mechanical properties of the sample.

Another well-studied hybrid process is plasma spraying with subsequent LT. In comparison with the laser source, the plasma source is less concentrated but more powerful and economical. Therefore, during laser plasma assisted spraying (LPASS) it is possible to achieve the fabrication of high-strength coatings with a sufficient cohesion to the substrate. Lately, there has been a great deal of interest in the combination of a cold spray with LT [2,3]. In the first stage of the laser-assisted cold spray (LACS) process, the FG coatings on the substrate are produced due to the mechanical embedding of the accelerated powdered particles. In the second stage, these FG layers undergo a precision laser remelting, resulting in improved adhesion between dissimilar layers, owing to the creation of chemical bonds and new compositions, in the increase of the coating strength and in the emergence of new and interesting mechanical properties.

In papers by Shishkovsky *et al.* [4], the possibility of a selective laser sintering/melting (SLS/M) process and LC of exothermal powdered mixtures, traditionally applied in self-propagated high-temperature synthesis (SHS), was shown for the first time and theoretically confirmed [5]. Thermal-physical modelling of the SLS/M + SHS and LC + SHS processes will be considered further in Section 11.5 of this chapter, and in Section 11.4 we will describe experiments on the thermal field measurement in the combustion front under such a hybrid combination.

11.2 Laser control of self-propagated high-temperature synthesis (SHS) as synergism of the two high-tech processes

11.2.1 Self-organization under SLS on exothermal powder composition

When realizing the combination of the LI and the SHS processes, it is necessary to make sure that the controllable exothermal combustion reaction takes place exactly within the spot of the LI, scanning by the powdered composition surface, because only the spaced-selective cladding with high-resolution allows a synthesized object to take a tightly defined shape. This answers the long-term objective of 3D synthesis. The SHS process realized by the SLS/M or LC methods created not only stronger material copies of the complex form [6], but also increased the functional features of these 3D objects, owing to the new phases synthesis (intermetallics, piezoelectric, and ferroelectric, etc.).

We were the first to offer and realize the laser-controlled combination of the SLS/M + SHS processes in the overall technological process using the following powdered compositions [1]:

- metal mixtures for the intermetalide synthesis in systems Ni + Ti, Ni + Al, Ti + Al, Fe + Ti, Fe + Al, Cu + Al + Ni;
- mixtures of metals in the gas phase/analogue of a laser chemical vapor deposition process: Ti + N₂, Al + N₂, Ti + O₂;
- oxide's metal mixtures for the ceramics synthesis TiO₂ + ZrO₂ + PbO, Al(Al₂O₃) + Zr(ZrO₂);
- laser-controlled synthesis of barium hexaferrites and lithium ferrites-spinels from BaO₂ + Fe₂O₃ + Cr₂O₃ + Fe, Li₂CO₃ + Fe₂O₃ + Cr₂O₃ + Fe.

Optimal LI regimes for the maintenance of the controllable exothermal reaction exactly within the laser spot were determined. For some systems, the 3D samples made of the above-mentioned compositions were obtained. In this chapter we will discuss the synthesis of intermetallic phases, in particular aluminide of titanium, nickel, and iron in the matrix of the main metal under the layerwise LC.

Among other things, the originality of our approach consists in the fact that the LI is not just reduced to an additional and precise thermal energy input, as in cases for the LPASS and LACS [7,8]. A special frequency and amplitude selection of the external field with respect to the natural oscillation frequencies of the “powder

mixture + synthesized sample” system, can initiate a number of phenomena of the resonance nature. The LI as one of the methods for achieving this resonance state is easily controllable, power consuming, and has a point nature, that is, it is extremely challenging as the source of the external electromagnetic fields. On the whole, the problem of self-similar phenomena, which can arise in such experiments, is interesting by itself and deserves a special separate examination. Note that self-similarity is not the same as self-organization. If we have a coherent structure, and the laser has a coherent property, and the LI acts beyond the multiphase systems, this is one of the conditions of the appearance of the self-organizing media.

The combination of laser alloying with the ultrasonic treatment considerably improves the physical-mechanical properties of the end product, due to the cavitation processes in the liquid phase. The selection of the amplitude and frequency of the ultrasonic vibrations is determined as far as the conditions for the standing acoustic wave’s formation in the laser melting zone.

The LI is an electromagnetic wave with its own amplitude and frequency. In contrast to usual light sources, the LI possesses unique, fundamental physical properties. These are monochromaticity, space and temporal coherence, narrow LI directivity, and strict polarization. If the last two of the LI’s properties are used in the laser technology, then the wave properties are not mentioned. However, considering the ultradispersed (nanodimensional) powders, aerosols (i.e., when particle size is comparative to or less than the light wavelength), and the wave nature of the LI (its amplitude, frequency, and phase) begins to play a not insignificant role. So it is possible to govern such structures by means of the LI parameter variation.

The variation of depth (h) of the SHS reaction against specific laser energy input (A) is shown in Figure 11.1. It can be noted that with increasing A the values of h tends to also increase. If A is increased beyond the limit shown in Figure 11.1, this results in an uncontrolled thermal explosion across the entire volume of the sample. In the case of lower values of A (below that listed in the figure), the layers are incompletely sintered and lead to a mechanically weak, friable composite. It is important to note that the slopes of the plots characterize the rate of power supply that is suitable for sustaining the SLS/M process.

For Ni powder of PGRS-4 grade, the h value is greater than that for pure Ni. It is also clear that the impurities present within the PGRS-4 grade of Ni powder tend to strengthen the sintered layer. Fine Ti powder (PTOM grade 98-99 wt.% Ti) exhibits a higher level of reactivity than the Ti powder of higher purity 99.2 wt.% Ti (Figure 11.1, curves 3 and 4). Therefore, combinations of these powders can also be used to influence the SLS process. As can be seen from Figure 11.1, the process is markedly affected by the composition of the starting mixture. For the Al+Ti mixtures 1:1, and 1:3 stoichiometric ratios in air, and 3:1 in N_2 (absent in Figure 11.1), no controlled SHS-SLS was achieved. The slopes are indicative of different energy consumption levels in the respective reactions (compare curves 3 and 6 in Figure 11.1). Curve 7 (Figure 11.1) refers to the synthesis of the hexaferrite $BaFe_{12x}Cr_xO_{19}$ from a mixture of metal and oxides.

Calculated in [4], induction periods for P , V , and D imply that the Ni_3Al synthesis takes place only within the laser beam spot. The spot diameter (about 60 μm) is

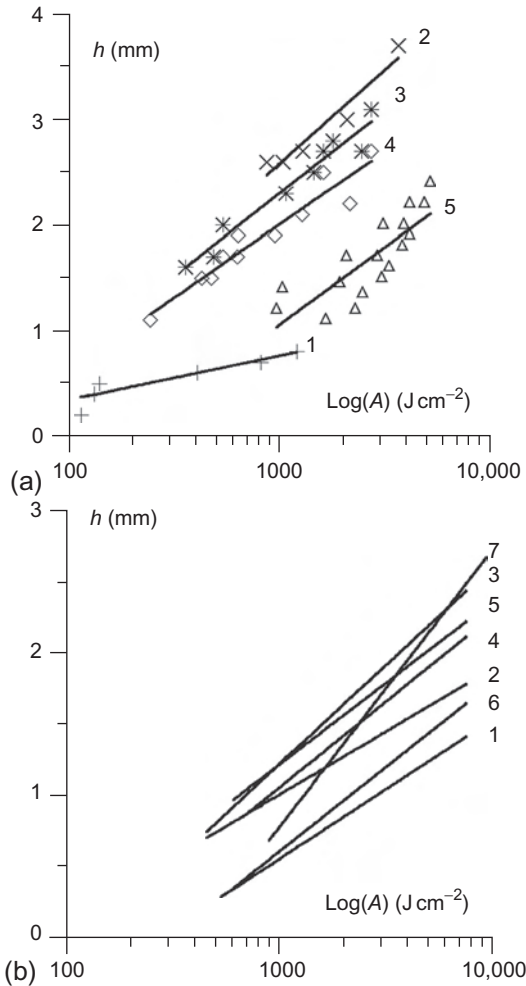


Figure 11.1 The depth of laser-controlled sintering h versus $\log A$ for [7]: (a) (1) Ni+Al (1:1), (2-4) Ni+Ti (1:1), (2) PGSR4+PTH, (3) PGSR4+PTOM, (4) PNK+PTH, (5) PZT. (1, 2, 5) SLS on air, (3, 4) under Ar and (b) (1, 4, 6) Al+Ti (3:1), (2, 5) Al+Ti (1:1), (3) Al+Ti (1:3), (7) $\text{BaFe}_{12}\text{Cr}_x\text{O}_{19}$. (1-3) SLS on air, (4, 7) under Ar, (5, 6) under N_2 .

comparable with D and the particle size of the starting powder. X-ray diffraction (XRD) data for the Ni-Al and Al-Ti systems confirm the formation of the respective aluminides. The energy activation of the SHS reaction in the system Ni-Al is significantly higher than in systems Ni-Ti, Ti-Al, so the synthesis process in these systems are badly controlled (see data presented in Tables 11.1 and 11.2). Titanium aluminide under 3D SLS/M+SHS also poses some challenges (Figure 11.1). In particular, the system Al-Ti “burns” practically on all regimes in the N_2 and/or Ar as on the air, and from this it has been noted that the Al_xTi_y synthesis requires a careful preparation of mixture (which requires oxygen and nitrogen to be removed from pores).

Table 11.1 Thermophysical parameters of the Ni-Al system

Phase	T_i (°C)	E (kJ/mol)	Q (J/kg)
Ni ₂ Al ₃	–	–	1.9×10^6
NiAl	910 ± 25	135 ± 27	9.7×10^6
Ni ₃ Al	925 ± 16	115 ± 25	2.4×10^6
(Ni + Al) Melt	–	48.24	1.3×10^6

Sources: [9,10].

Table 11.2 Thermophysical properties of the ignition reaction in the Ti-Al system

Initial powder mixture	T_i (°C) thermocouple/simulation		E (kJ/mol)	Q (J/kg)	X-ray comments
	Beginning	End			
Al: Ti = 1:3	$645 \pm 10/-$	$1150 \pm 50/1244$ (adiabatic)	18.0 ± 1	–	Ti main, Al small, Ti ₃ Al, TiAl, TiAl ₃ minor
Al: Ti = 1:1	$645 \pm 10/-$	$1400 \pm 50/1245$ (adiabatic)	19.5 ± 1	–	Ti ₃ Al main, TiAl, TiAl ₃ small
Al: Ti = 3:1	$645 \pm 10/-$	$1200 \pm 50/1271$ (adiabatic)	22.5 ± 1	–	Al main, Ti, TiAl ₃ small

Sources: [11,12].

What are the main reasons for conducting the SHS reaction under the LI? The specific characteristics of laser energy dosing for the SHS process is such that (1) it is impossible to consider the laser influence as a heat source only, particularly when using it in the case of soot; (2) the laser influence is a high-energy source (temperature gradients and heating-cooling velocities are comparable and can exceed SHS energy); (3) it is impossible to allow for a united macro front of the SHS reaction under the selective LI, as this process will become uncontrolled and it is impossible to fabricate the 3D object; and (4) temporary and spatial LI shape are not comparable with traditional types of heat sources (such as plasma, arc, and induction heating). Under experimental conditions, a heat explosion has been observed when the laser control under SHS process was lost.

Experimental heat situation studies in the LI area for exothermal powdered mixtures (Section 11.3) [13,14] and a detection of electromotive force occurrence on the combustion front [8] indicate that we have a deal with “laser-controlled” high-temperature syntheses (LHS) of new chemical compounds (more information on this

is given in the chapter on aluminides of the Ti, Fe, and Ni) from the initial mixtures of reactionary powders with stoichiometry ratios.

11.2.2 Thermophysical estimations and fractal behavior for laser-controlled high-temperature syntheses

Analysis of the intermetallic phase substructure synthesized after the SLS/M+SHS overlapping gives very interesting results under great magnification (Figure 11.2). The intermetallic surface has a brightly denominated fractal order. Such order is observed at the LI regimes with a high-energy input. Moreover, such ordering on the elementary level has also been observed under the SLS/M+SHS overlapping. The SLS/M process of prealloying intermetallide (for instance, nitinol graded PN55T45) gives the traditional liquid phase sintered morphology.

The formed nanostructures present an interesting object itself for the study of the system behavior with lowered dimensionality. However, geometric shapes of synthesized nanostructures in reactionary-capable Ni-Ti, Ni-Al, or Ti-Al powdered systems are, in principle, different.

The fine structure in the intermetallic compounds on the micro- and the nanoscale after the SLS/M+SHS overlapping will determine the successful applications of the 3D articles. This area requires further investigation. As it was noted in [4,13,14], there is a clear correlation between the LI parameters and the morphological structure of the sintered surface under the layerwise laser synthesis of intermetallic compounds. It was shown in [11] that the high degree of nitinol implant osteointegration has a great deal of influence on the developed sub- (nano-) structure of porous implants.

The evolution of the micro- and macrostructure (surface morphology), depending on the laser processing parameters, can be tracked through analysis of the fractal dimension of the structure, D [15,90]. It is obvious that the transition from the nano- to the micro- and macrostructural levels (by process of the atom-by-atom droplet formation under rapid crystallization of the melt) can be interpreted as percolation threshold, that is, the transition of the material to a state when the connection between individual particles (atoms) can be described as fractal cluster formation and segregation. Evolution of the percolation cluster is governed by structurally sensitive characteristics such as pore size, roughness, and specific surface area, dissipative structures appearing in the course of the structure formation, and coagulation and recrystallization processes. At the same time, the formation of new intermetallic phases under SLS/M+SHS can also lead to additional changes in D . Because the nucleation periods under structural phase transition and in the course of the molten pool crystallization are different, variations of D should occur [16]. With the increase of the nucleation rate (i.e., laser cooling rate) the percolation cluster's structure becomes more compact while the fractal dimension tends to the Euclid's universal one [17]. In other words, the fractal dimension characterizes the degree of surface roughness.

Highly magnified images of the typical microstructures obtained in Ni-Al, Ti-Al, Fe-Ti, and Ni-Ti systems under SLS/M+SHS are presented in Figure 11.2. It can be

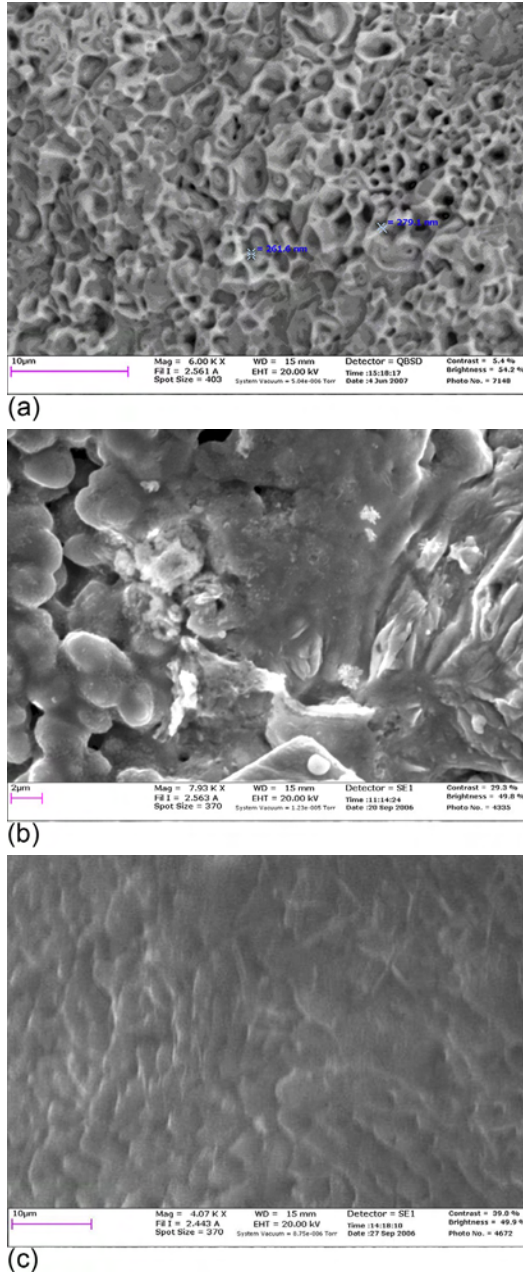
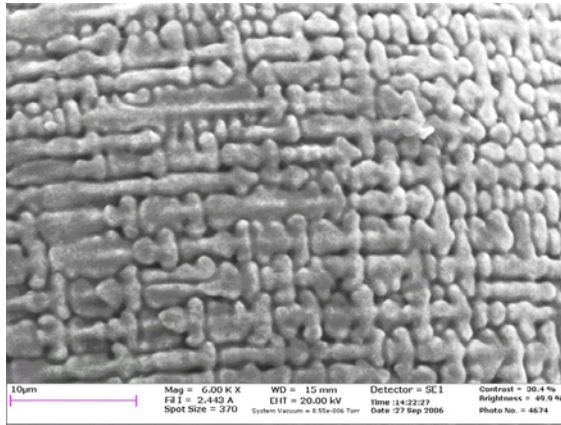
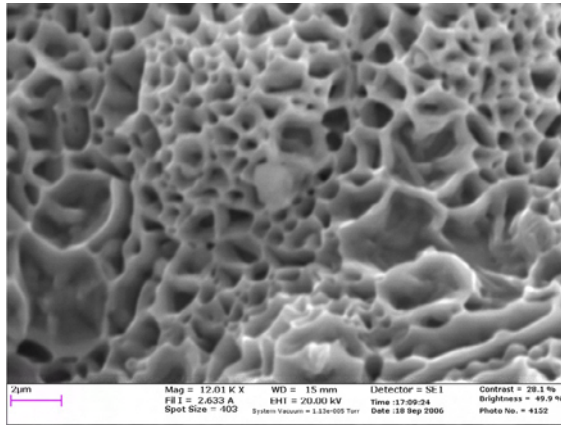


Figure 11.2 Microstructure of the intermetallic synthesis during SLS/magnification and accelerating voltage are shown on pictures, laser beam diameter $L_b \sim 100 \mu\text{m}$: (a) Fe-Ti = 1:1, $P = 17.8 \text{ W}$, $v = 2.8 \text{ cm/s}$; (b) Ni-Al = 1:1, $P = 30.3 \text{ W}$, $v = 2.8 \text{ cm/s}$; (c) Ti-Al = 3:1, $P = 15.2 \text{ W}$, $v = 1.5 \text{ cm/s}$;

Continued



(d)



(e)

Figure 11.2 Continued. (d) Ni-Al = 3:1, $P = 30.3$ W, $v = 11.4$ cm/s; and (e) Ni-Ti = 1:1, $P = 13.9$ W, $v = 5.7$ cm/s [11].

seen that there is a certain correlation between the shapes and the sizes of the obtained substructures (cf. Figure 11.2a, e and c, d). Further on, the intermetallic phase formation process will be analyzed on the basis of the phase diagrams of these systems.

According to the equilibrium phase diagram (EPD) of the NiAl system [4,9], the following phases are observed at the different heating and cooling stages. Under heating to temperatures up to $T_e = 640$ °C, the metastable Ni₂Al₃ γ -phase emerges and grows. With further heating, γ - and δ -phases coexist, then in the interval of 1132 °C $< T < 1638$ °C the γ -phase melts and the NiAl δ -phase remains. Finally, only upon reaching the melting point of the NiAl intermetallic ($T_3 = 1638$ °C), the NiAl phase, followed by the Ni₃Al ε -phase emerges in the subsequently cooled melt.

Therefore, depending on the selected LI parameters (P , v , L_b) and the mixture composition, laser irradiation energy may be sufficient or not to achieve the appropriate temperatures and to obtain intermetallic phases predicted by the EPD in the SLS/M + SHS synthesized part. At the same time, a principle difference in the fine substructure in the Ni-Al (1:1) system in Figure 11.2b and in the Ni-Al (3:1) system in Figure 11.2d is evident. Dendritic structure of the NiAl system and mosaic structure of the Ni₃Al system indicate the varying character of the transformations under synthesis of these intermetallic compounds. It can be assumed that these differences in the ordered low-dimensional clusters are induced, among others, by the above-described phase formation conditions.

The EDX microanalysis cannot provide the type of the intermetallic phase, but the presence of phases such as Ni₃Al and NiAl may be established based on the quantitative content of these elements. X-ray phase analysis (XRD) results reported in Ref. [12] (see Section 11.3.3 also) and theoretical assessments in Ref. [1] showed that under laser-controlled synthesis, it will be more advantageous to obtain the Ni₃Al intermetallic phase compared to the NiAl one, as the former is steady. It may be related to the fact that the NiAl phase synthesis reaction is accompanied by a considerable heat release while the formation of this phase starts later than the Ni₃Al one's [4,9].

The XRD, SEM, and backscattered electron microscopy (BSEM) methods were applied in Ref. [18] to establish the sequence of the phase formation in the TiAl system under the temperature increase, including that induced by LI (cf. thermocouple measurement in Ref. [13,14]). It was shown that upon reaching $T = 645 \pm 10$ °C, the reaction of combustion and synthesis of Ti_xAl_y phases (where $x, y = 1, \dots, 3$) takes place at the boundary melt (Al)/solid (Ti) in the contact area of melted aluminium. As a result, an intermetallic frame consisting of Al₃Ti is formed with the subsequent TiAl phase synthesis from noncombusted Al and Ti. This type of microstructure is presented in Figure 11.2c. There is a certain similarity in the appearance of the substructures in Figure 11.2c and d.

The melting and exothermal reaction in the Fe-Al system starts at the boundary between Al and Fe and probably with participation of its oxides (Fe₂O₃, Fe₃O₄). This reaction is called a termite one. The yield of this reaction consists of Fe_xAl_y intermetallic compounds, and probably the alumina formed during the synthesis reaction, while the Al-Fe percentage diminishes [19]. The exothermic heat emission facilitates accelerated melting. The reaction mechanism involves not only the decrease of Fe, the conversion of Fe₂O₃ to Fe₃O₄ and FeO, and the oxygen release, but also aluminium oxidation, interaction of Al with the iron oxides, the formation of the complex Al-Fe-O, Al₂O₃ oxide phases and Al-Fe intermetallic compounds proper, depending on the reaction temperature and Fe/Al ratio in the mixture.

During the high-speed laser cooling, the alloys with the aluminium content up to 34 at.% from the high to room temperatures they acquire the structure of α -solid solution. In the alloys with the Al content ranging from 34 to 52 at.%, the FeAl₂ structure is exclusively observed. Under the higher aluminium percentage, the different intermetallic compounds (FeAl₂, Fe₂Al₅, FeAl₃) are formed. The ordered structure of the Fe₃Al type is formed in the alloys containing from 25% to 34% of Al, after a slow cooling. After the quenching of these alloys at the temperature of 600 °C and above, the

FeAl₂ structure appears. The ordering process is characterized by a change in the number of physical properties, in particular, by a lower value of the Curie point, by a change in the crystal lattice spacing at room temperature depending of the content of Al. With its content up to 10 wt.% the crystal lattice spacing increases linearly with the increasing in the content of the alloying element. In the ordered state, the alloys with the Al content ranging from 10 to 20 wt.% are characterized by almost constant lattice spacing.

Finally, the Fe_xTi_y and Ni_xTi_y intermetallic phases are synthesized in the equiatomic systems FeTi and NiTi [1]. The Ti₂Fe, TiFe₂, and Ti₂Ni metastable phases may occur as well, respectively. As can be seen in Figure 11.2a and e, the similarity in the trend of the processes leads to the formation of resembling substructures.

The wall thickness h of the ordered honeycomb-like nanostructures typical for the Ni-Ti and Fe-Ti systems versus laser energy input is plotted in Figure 11.3. The wall thickens and diminishes with the laser energy input increase, and the substructures become more openwork. As for substructures in the Ni-Al and Ti-Al systems, such boundaries (honeycombs) are hard to distinguish.

The fractal dimension D is plotted in Figure 11.4. The varying character of the D change under the increase of the laser energy input A should be noted. D grows in the system Ni₃Al that indicates a more complicated character of such nanostructures (cf. also Figure 11.2d). A similar behavior of $D = D(A)$ was observed in Ref. [8] concerning the fractal dimension of pores under SLS/M of pure titan. Both increase and decrease of D occurred in the Ni-Ti and Fe-Ti systems. Variations of the D orientation indicate a change of the phase formation mechanism, that is, the metastable Ti₂Fe, TiFe₂, and Ti₂Ni phases give place to the more steady TiFe and TiNi intermetallic phases, respectively. It was found that the reactive capability of the NiAl system is

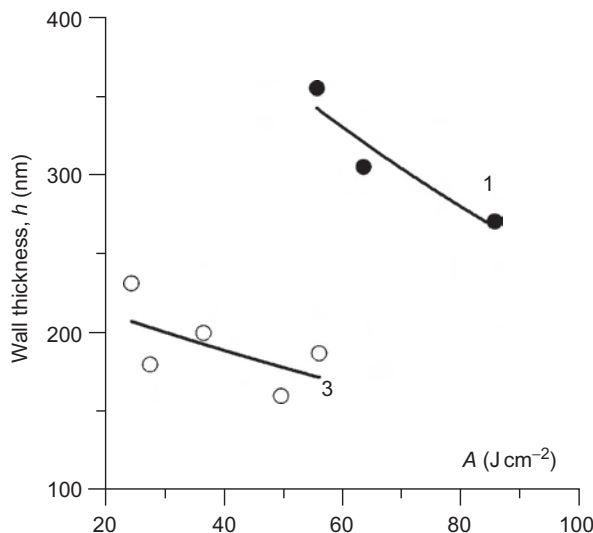


Figure 11.3 Dependence of the nano wall thickness h (nm) on laser energy input A (J/cm²): (1) Fe-Ti and (3) Ni-Ti [11].

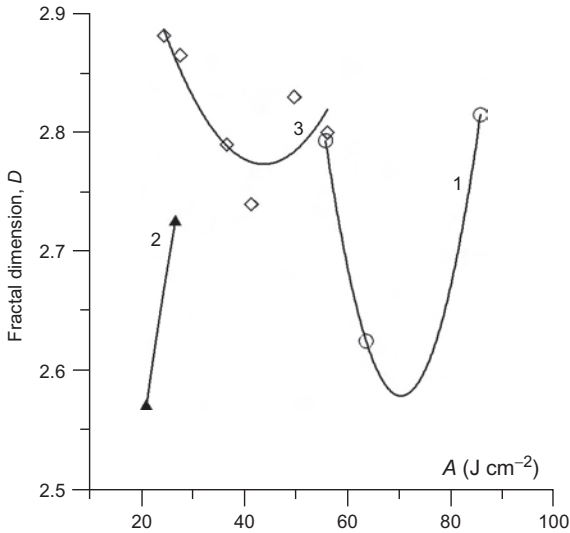


Figure 11.4 Fractal dimension D versus laser energy input A (J/cm^2): (1) Fe-Ti; (2) 3Ni-Al; and (3) Ni-Ti.

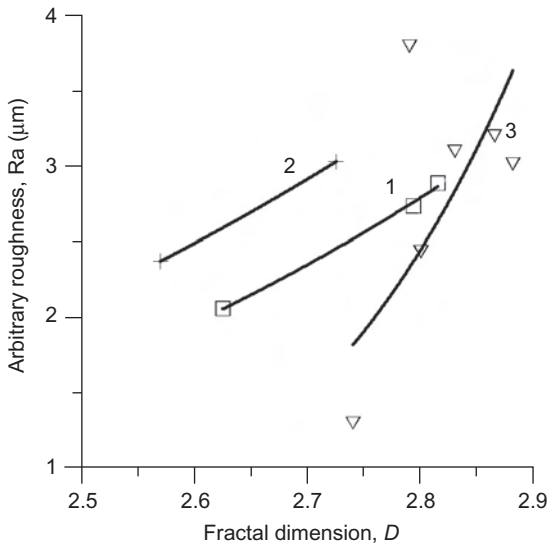


Figure 11.5 Arbitrary roughness R_a (μm) versus fractal dimension D [11].

enhanced and D increases when PGSR4 powder is replaced by pure nickel. The highest $D=2.91$ was observed in the NiTi system at $P=13.9$ W and $v=3.8$ cm/s. [Figure 11.5](#) plots the nanosurface roughness versus the fractal dimension. Thus, it was shown that fractal dimension is a structure-sensitive parameter characterizing the degree of self-similarity of irregularities of different sizes [8].

Thus, the hybrid combination of the SLS/M+SHS and LC+SHS processes is characterized as far as the synergetic effect, which is evinced by obtaining not only functional articles, but also to reaching the synthesis conditions of new intermetallide phases and structures ordering on all levels from the nano- to the microsized of crystallites.

11.3 Overlapping of laser cladding and SHS processes for the fabrication of the functional graded (FG) iron, nickel, and titanium aluminides in the surface layers

As was noted in [Section 11.2](#), we experimentally approved the layerwise laser melting and cladding process in the Me + Al (Me = Ti, Ni or Fe) systems [4,12,20–22] and theoretically substantiated [23] the approach, where the strengthened intermetallide is created directly within the LAM process in the metallic matrix due to the synthesis reaction. Nickel aluminides NiAl and Ni₃Al are characterized by high heat resistance, including the conditions of high-temperature gas flows. The intermetallic compounds in the Al-Ti system are promising materials for the manufacturing of high-temperature and radiation-resistant coatings. Titanium and nickel aluminides can be used as a carrier matrix for catalytic additives. Titanates of iron are promising in hydrogen power engineering, and nickel titanium is widely known as a biocompatible material.

The LI initiates a chemical reaction between the particles in the powder mixture of stoichiometric composition, thus leading to the intermetallic phase, and the excess substance (a deviation from the stoichiometry) aggregate the material matrix. The synthesis reaction realization is advantageous due to the finer and more uniform distribution of the inclusions in the crystalline structure, its internal stability, and the additional release of the exothermic reaction energy under the structural-phase transformations. The LI does not only activate the synthesis reaction, it also contributes to the acceleration of crystallization and governs the properties of the intermetallide microstructures ([Figures 11.3–11.5](#)). By controlling the poured layer thicknesses (i.e., the volume of the reaction zone) this can influence the motion of exothermic synthesis reactions and the solidification process (due to the change in thermal conditions), and can also have an influence on the size and shape of the microstructures. Furthermore, the laser power and scanning speed also affect the melting-crystallization conditions.

Functionally graded structures (FGS) and FG objects fabricated by applying complex and dissimilar materials ensure the specific properties of the final product. The manufacturing of 3D FG objects by the 3D LC and/or direct metal deposition (DMD) is one of the most promising techniques capable of meeting various industrial challenges [24,91]. This approach permits new freedoms in design and manufacturing, thus allowing, for example, to create an object with the desired shape, internal structure, and engineering composition, including the appropriate physical-mechanical properties, within a single-step fabrication process.

Because LI is reflected well by aluminium, the more refractory Me (Ti, Fe or Ni) must be the matrix material, and, in accordance with the Me-Al phase diagram, it should be expected that it will obtain the next stable intermetallide phases of

aluminides as— Me_3Al , MeAl , MeAl_3 (plus some metastable phases) in the exothermic reaction of the type: $x\text{Me} + y\text{Al} \rightarrow \text{Me}_x\text{Al}_y + Q$, where Q is the reaction thermal effect. Under the Al selection as the matrix basis, besides problems with the energy transfer from the LI to the material, another factor will appear. Aluminium has a low melting point in comparison with the refractory metal melting point (cf. 660 against 1537 °C for iron), and it will more effectively remove a heat due to the higher thermal conductivity, which ultimately will require a larger laser energy input.

The method of FGS fabrication used in the present study is schematically presented in Figure 11.6. The hatching distance was 2 mm, the layer depth was ~ 1 mm, and the powder feeding rate was ~ 10 g/min. The layers were made out of $\text{Me} = (\text{Ti}, \text{Fe}, \text{or Ni})$ and Al powders on a related substrate by the following strategy: the first two layers were of pure Me, the next two consisted of 70% Me + 30% Al, the third couple of layers were of 50% Me + 50% Al, and lastly the upper 7th and 8th layers had the ratio of 30% Me + 70% Al. Each second layer was formed on the bottom layer after its turning by 90°. Argon was the carrying gas. The laser scanning speed was 500 mm/min, laser power varied within the range of 800–1200 W, and laser beam spot diameter was 3 mm. The first channel of the feeder with the Me powder had a gas flow rate of approximately 20 l/min while the second one with the Al powder was ~ 10 l/min.

In Figure 11.7 the results of the layer-by-layer 3D synthesis are presented, and the LI passages are clearly visible. In the areas where the LI starts and at the turns from one passage to another, the laser beam speed is slowed down (as showed by the pointers in Figure 11.7a), and the heat dissipation speed is substantially less than in the central areas, thus leading to the cladded boundary obstruction and degradation

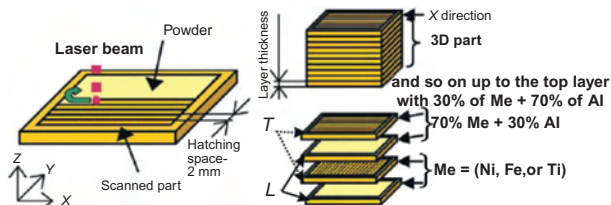


Figure 11.6 Schematic of the multicomponent graded structure fabrication by 3D laser cladding. Longitudinal L and transversal T [22].

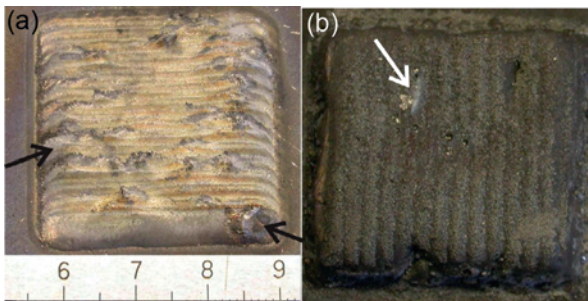


Figure 11.7 Sample fabricated DMD process: (a) Ti-Al; (b) Fe-Al. Arrows indicate problem areas on the laser cladded surface.

(Figure 11.7b) of the physical and mechanical properties of the structures being synthesized.

11.3.1 Laser synthesis in Ti-Al system

Gamma alloys of titanium aluminides in the Ti-Al system have been developed for high-temperature applications in the automotive, aerospace, and power generation industries [25]. The TiAl-based intermetallics have a number of advantages over the conventional titanium alloys; they are a higher elasticity modulus, lower density, and have better mechanical properties at high temperatures [26,27]. In our studies [20,21] the possibility of the laser-induced reaction synthesis of Ti_xAl_y intermetallics during the 3D laser sintering or cladding was asserted.

In accordance with the phase diagram, we expected to obtain the following stable intermetallic phases of aluminium titanates: $TiAl_3$, $TiAl$, Ti_3Al in the exothermic reaction of the type $xTi + yAl \rightarrow Ti_xAl_y + Q$, where Q is the thermal reaction effect. This system is widely used in the SHS technology, and its fundamental thermo-physical characteristics (T_i —an ignition temperature, E —the energy activation of chemical reaction, Q_i —the thermal effects of exothermic reactions on one mole) and synthesized phases are known (see Table 11.2).

The following powders were used in the experiments: a titanium powder was TiGd2 grade 99.76 wt.% Ti; and aluminium was grade 99 wt.% Al. Both powders are produced by the TLS Technik GmbH&Co. The powder particles were mainly spherical with a size of ~ 80 - $100 \mu m$ for 95% of them. The substrates were round plates with a 65 mm diameter and 5 mm height made of Ti-6Al-4V. The powder size distribution was studied by means of a granulomorphometer ALPAGA 500NANO (OCCHIO s.a.).

The results of the optical metallography are presented in Figure 11.8. A series of photos show the characteristic microstructures based on the lower, middle, and upper

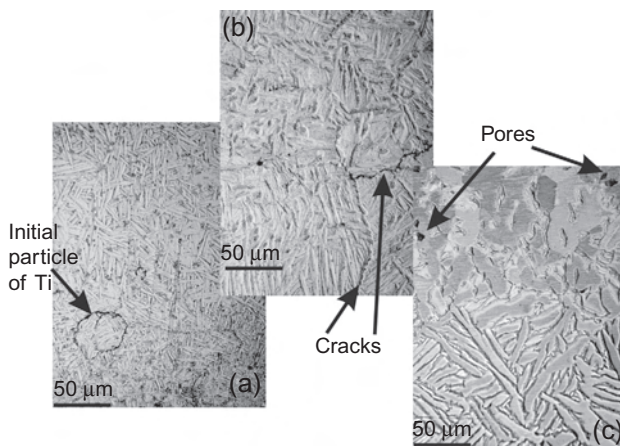


Figure 11.8 OM micrographs showing the typical microstructures of 3D laser clad coating of Ti-Al multilayer system in Ar: (a) bottom layers ~ 250 - $300 \mu m$ from substrate; (b) middle layers ~ 900 - $1000 \mu m$ from substrate; and (c) top layers ~ 1700 - $1800 \mu m$ from substrate [21].

parts of the 3D laser cladged FG volume, that is, where the proportions of the powdered Ti+Al \approx 3:1; 1:1, and 1:3 by weight ratios were comprised.

In the lower layers in the photo (Figure 11.8a), a predominantly lamellar microstructure typical of the single-phase titanium alloys with changing morphology can be observed. In the middle layers, mainly a coarse-grained structure occurs of the “basket netting” type. In the individual sections of near-surface layers, a fine grain is present with the martensite morphology of the β -titanium phase. The pointer in Figure 11.8a shows a nonremelted particle of the initial titanium. The existing structural heterogeneity is obviously connected with the nonuniform alloying, the exothermal reactions of the intermetallic synthesis, and high-speed laser cooling during the crystallization from the melt. In the lower and middle layers, subjected to a longer laser heating after solidification, the recrystallization features of α -Ti phase are observed. These plates were etched less clearly, so against their background the dispersed precipitations of the second phase (α_2 -Ti₃Al phase) appeared (Figure 11.8b).

These intermetallic phases, being more durable, cause the crack development at the grain boundaries (see Figure 11.8b). Finally, after the LC the upper layers are characterized by the coarse elongated grains of a dendrite type.

The measured microhardness (Figure 11.9) of the cladged layers grows from the substrate to the top irregularly. We believe this to be connected with a local hardness increase in the intermetallic phase locations. As a whole, the microhardness values correspond to similar measurements on the titanium aluminides after the DMD and LENS processes [26].

The X-ray analysis results are presented in Figure 11.10. The lower curve in Figure 11.10 corresponds to the diffractogram of the initial powder Ti+Al = 1:1 mixture without any treatment. As seen from the lower curve, the most intensive lines belong to (111) α -Al and (101) α -Ti, still a weak (101) line of β -Ti phase is also visible. These intensive lines of the initial phases completely disappear after the 3D laser cladding. However, there remains a sufficient number of the weaker lines against the large angles of α -Ti (110), (112) and, probably, of aluminium (220), (222). The

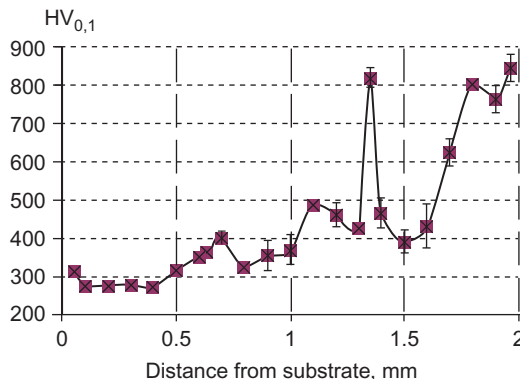


Figure 11.9 Microhardness distributions of Ti-Al FG multilayer system in argon [21].

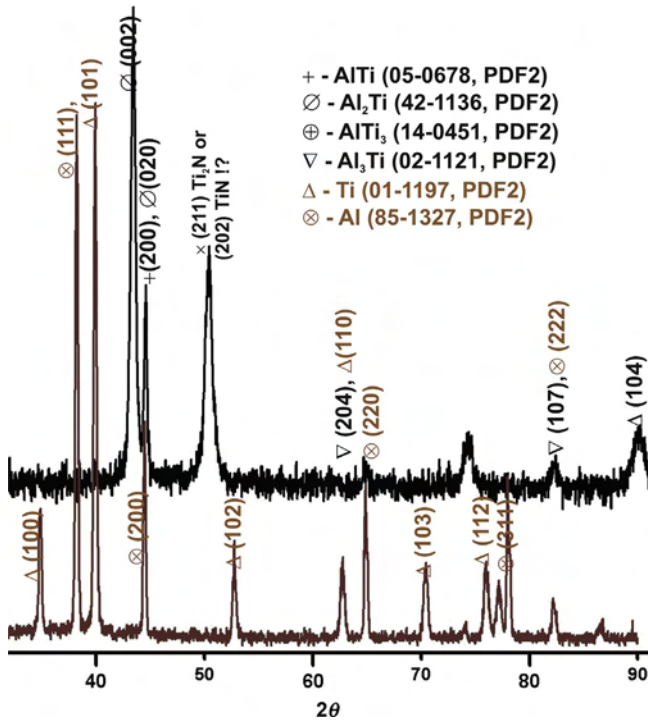


Figure 11.10 X-ray diffraction patterns of Ti-Al DMD multilayer system in argon. Lower curve is diffractogram of the initial Ti+Al = 1:1 powdered mixture without laser treatment.

presence of these lines attests to the fact that after the DMD process the Ti and Al initial phases have not reacted completely even in the case of the noncontrollable combustion in nitrogen (Figures 11.4b and 11.7b). After the DMD, the strongest lines are located at the angles of $2\theta \sim 43\text{--}45^\circ$, which in our opinion corresponds to the entire set of intermetallic phases. This is mainly a metastable phase (002), (020) of Al_2Ti and eutectic tetragonal (200) phase of $\gamma\text{-AlTi}$. A similar picture was observed in research reported in [26]. Furthermore, at the large angles we identified the lines (204), (107) of a tetragonal Al_3Ti phase. However, because their intensities are not great, the presence of this phase is doubtful. The element analysis data (Figure 11.11) confirm this suggestion. The presence of the nitrogen associations (200)— Ti_3AlN , disputably (200)— Ti_3AlC should also be mentioned. These are probably the intermetallic phases enriched with nitrogen and carbon. We assumed their presence in the Ti-Al system after the DMD process in nitrogen environment [21], while it was amazing to discover the occurrence of a strong peak near the angle of $2\theta \sim 50^\circ$ in the protective Ar medium. We consider them as nitride phases with lines (200) of the ϵ -phase TiN and (211) Ti_2N .

On taking into account all the peaks mentioned above, it is reasonable to conclude that this XRD pattern (Figure 11.10) best of all coincides with the set of lines for the TiAl intermetallide. This means that out of all the assumed stoichiometric (3:1, 1:1,

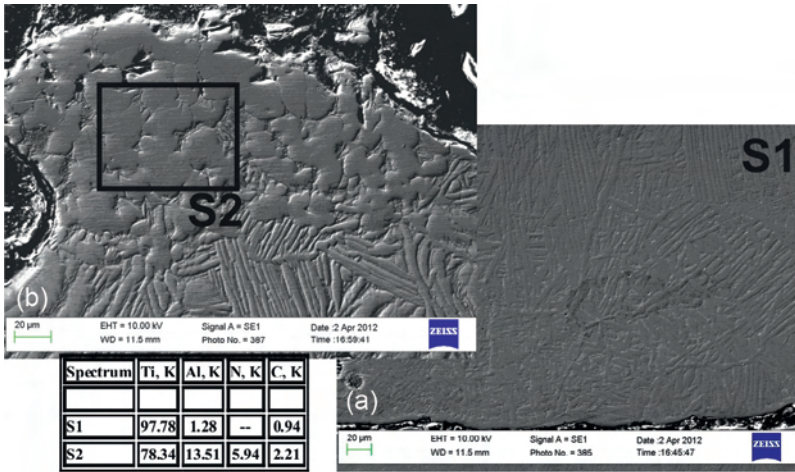


Figure 11.11 SEM micrographs showing typical solidification microstructures of clad coatings with laser scanning speed of 0.83 cm/s and 400 W with EDS result (S1 and S2 regions) of Ti-Al multilayer system in Ar: (a) bottom layers near substrate and (b) top layers [21].

1:3) mixtures, the combustion reaction of the Ti_xAl_y intermetallic synthesis was going by the following direction: $Al + 3Ti \rightarrow AlTi + 2Ti$. This explains both the presence of a large number of residual nonreacted Ti powder and a very low quantity of pure aluminium.

The SEM images of the micro- and substructures are shown in Figure 11.11, just as in Figure 11.8, from the lower, middle, and upper parts of the clad layers.

On the whole, their images corresponded to the optical metallography data given above. However, the results of element analysis are the most interesting. They show that, despite the fact that the FGS scheme assumed introduction of up to 50% of Al in the middle layers and more than 80% of Al in the upper layers, this aluminium was practically not fixed. It is possible to suggest that the temperature was enough to evaporate the aluminium, which is why we observe it now on the microphotograph (Figure 11.8) in the form of a whitish coating.

Because the solid but brittle AlTi, AlTi₃ intermetallic phases identified by us are the second phase inclusions for the titanium matrix of clad layers, and thus simultaneous with the strengthening of the titanium matrix, they cause its cracking. This phenomenon was visually noted by the authors.

11.3.2 Laser synthesis in Fe-Al system

Interest aroused by the intermetallide phases of the Fe-Al system is connected with their high strength per unit weight, corrosive and wear durability, and low price of manufacture [28,29]. High-temperature applications for the iron aluminides include the pipeline of heat exchangers, turbine blades, the valves of complex shapes for

engines, and the substrates for catalytic converters [30–32]. The conventional fabrication method for solid 3D articles through the Fe-Al intermetallic compounds is casting, resulting in partial oxidation and grain growth due to high-temperature aging over a long period of time. The direct manufacturing of 3D articles of these materials is difficult, due to the brittleness at low temperatures inherent in those intermetallics. Furthermore, the subsequent sample-machining from the Fe-Al intermetallic compounds leads to more wear of the cutting tool than does machining with the usual Fe-C alloys.

Therefore, attempts have been made to obtain the Fe-Al intermetallic samples and coating by alternative methods, such as through thermal spraying, magnetron sputtering [33–35], SHS [36,37], and laser additive manufacturing (LAM) (3D laser cladding, DMD, LENS, SLM processes) [19,38–44]. Nevertheless, these methods also have a number of negative factors, which decrease the effectiveness of these approaches, such as porosity and high connection strength due to the difference in the temperature expansion coefficients of the coating and the base layer.

Of particular interest is the fabrication of the metal-the matrix composites (MMC), when the reinforcing Fe_xAl_y intermetallic compounds, are added to the matrix of the base metal (for example, Fe or Al). This process can be realized by several methods. Within the first approach, the preliminary addition of the strengthening prealloying intermetallic particles in the powder mixture occurs before the LAM process [22,40].

In the Fe-Al system this approach was approved in the papers [19,45], where the Al/Fe₂O₃ mixture was combined during the SLM process for the direct creation of articles through the aluminium matrix with the strengthening inclusions. It was shown that the SLM can ensure the homogeneous distribution of the alumina and Al-Fe(-O) particles. In a study [40], the SLM conditions for the prealloying FeAl intermetallic compounds were determined.

Another interesting direction is the laser welding of the dissimilar materials, that is, Fe and Al alloys, which are important for the aerospace and automobile industries for which serious difficulties are caused by the high brittleness of the intermetallic phases generated in the melting pool [46–50,89]. On knowing the succession of the phase-structural transformations in the laser weld joint, it is possible to attain the fabrication of such a barrier layer of the alloying elements (AE) [46–48] that is capable of wetting the joining alloys on the basis of iron and aluminium, protecting them from the contact during the melting and preventing the formation of undesirable phases. There are different methods for the plasticity improvement of such welded joints, including crystallographic structure modification, boundary strengthening, grain-size decrease, columnar structure creation, and micro- and macroalloying, and all of these methods can be completely realized using the LAM methods.

The powders enumerated below were used for the experiments. The iron powder had 99.76 wt.% of Fe (TLS Co.). The alloy 2024 (TLS Co.) was used as the Al powder, which had the following chemical composition: Cu 3.8–4.9, Mg 1.2–1.8, Mn 0.30–0.9, Si 0.50, Fe 0.50, Zn 0.25, Ti 0.15, Cr 0.10 wt.%, bal. Al. The powder particles were mainly spherical with the size of ~80–100 μm for 95% of them. Steel substrates of a square shape with a 50-mm width and 5-mm height were used. The FGS fabrication scheme in the Fe-Al system is shown above (see [Figure 11.6](#)).

Figure 11.12a-c represents the results of optical metallography. As before, the photo series was selected in order to exhibit the characteristic microstructures from the bottom (a), middle (b), and top (c) parts of the clad layers, that is, the parts where the weight ratios of Fe-Al in powder were $\approx 3:1$, $1:1$, $1:3$, respectively. The bottom cladding layers (Figure 11.12a) have a fine-crystalline structure with an almost uniform morphology mainly typical of single-phase iron alloys. In the middle layers (Figure 11.12b), the structure becomes more developed (see the supplementary inserts to Figure 11.12b1-b3), while in the lower layers (Figure 11.12b1) the transition from the fine-crystalline to the grain structure is observed. Further on, this grain structure (with typical grain size of $20\ \mu\text{m}$) transforms into the dendrite-type structure (Figure 11.12b3). Finally, in the upper layers (Figure 11.12c1-c3) an extremely heterogeneous MM structure is clearly visible, with the boundary intermetallic phases being precipitated (Figure 11.12c2). The dendrite nature of the Fe matrix structure testifies to the intensive overheating and the subsequent high-speed supercooling of the material in the LC process. In Figure 11.12b and c the cracks are arrowed, going in the direction of the layer and the direction of the main heat removal to the substrate base. Obviously, the observed structure heterogeneity is connected with the inhomogeneous intermetallic phases (Fe_3Al), alloying, and the laser supercooling regime, during the melt crystallization.

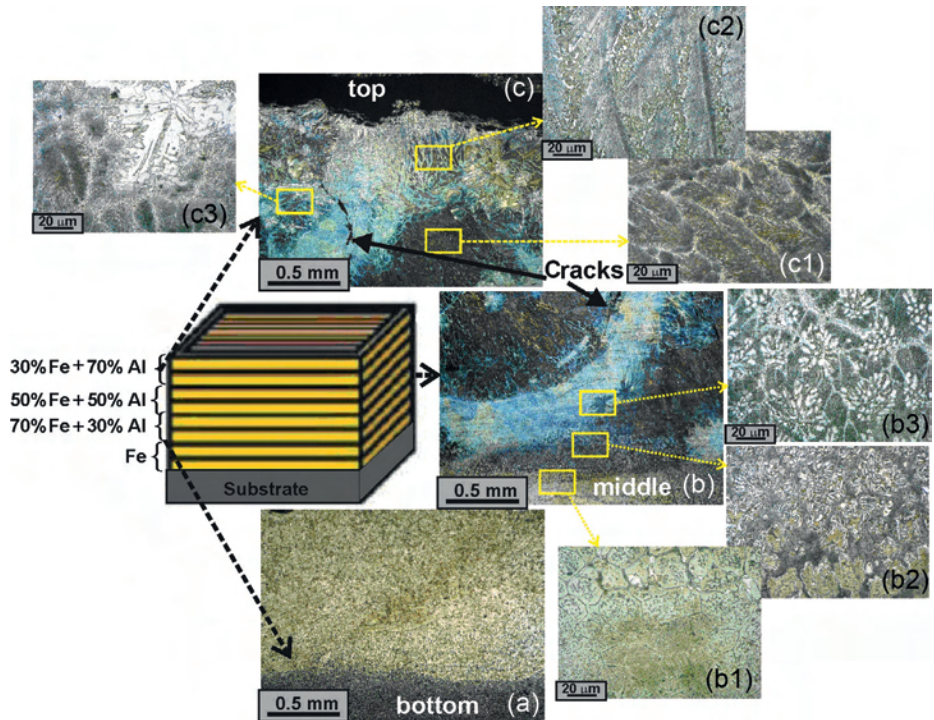


Figure 11.12 OM micrographs showing the typical microstructures of 3D laser clad coating of Fe-Al multilayer system: (a) bottom layers $\sim 2\text{-}4\ \text{mm}$ from substrate; (b) middle layers $\sim 4\text{-}6\ \text{mm}$ from substrate; and (c) top layers $\sim 6\text{-}8\ \text{mm}$ from substrate [22].

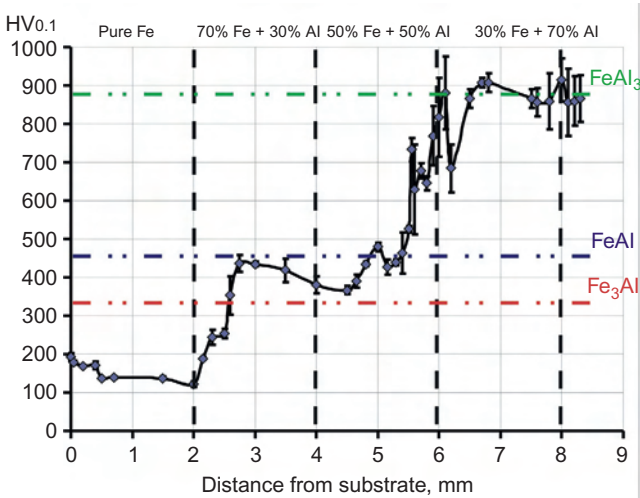


Figure 11.13 Microhardness distributions of Fe-Al FG multilayer system [22].

The formed intermetallic phases harden the iron matrix, but being low-plastic, they cause crack development along the grain boundaries (see [Figure 11.12b and c](#)). The measured layer microhardness ([Figure 11.13](#)) grows irregularly from the substrate to the top. We refer to this irregular growth as the local hardness increase in the locations of intermetallide phases. In [Figure 11.13](#), vertical dotted lines indicate the zones from the substrate surface, where the ratio and relationship of Fe and Al changed. Horizontal dot-and-dash lines designate the average microhardness level, characteristic of the Fe-Al intermetallic phases [51]. As follows from [Figure 11.13](#), the microhardness remains equal to 200 $HV_{0.1}$ within the layer from the substrate up to the 2-mm level. In the range from 2 to 6 mm it grows up to 300-500 $HV_{0.1}$ level and corresponds to the hardness of the Fe_3Al and FeAl intermetallide phases. Finally, in the last section from 6 to 8 mm the microhardness grows up to 700-900 $HV_{0.1}$, which is characteristic of the $FeAl_3$ phase.

It is known from the literature [51] that the Al_2Fe and Al_3Fe_2 metastable phases can have a microhardness of up to 1058-1070 and 1000-1150 $HV_{0.1}$, respectively. The microhardness dips we connect with the cracks on the grain boundaries. On the whole, the microhardness values correspond to similar measured values for the iron aluminides after the laser welding.

[Figure 11.14](#) shows the results of the X-ray analysis. The lower curve in [Figure 11.14](#) corresponds to the diffractogram of the initial 1:1 ratio Fe + Al powder mixture that has not undergone any treatment. As is evident from this curve, the most intensive lines belong to (111) α -Al and (110) α -Fe, although a weak line (200) of β -phase is also visible for the iron. After the LC, the intensive lines of Al disappear completely, while the Fe lines are probably “hidden” behind the intermetallic compound lines at angles of 44.6° and 64.7°. This result testifies to the fact that, after the LC, the entire amount of Al has completely reacted into the exothermic reactions

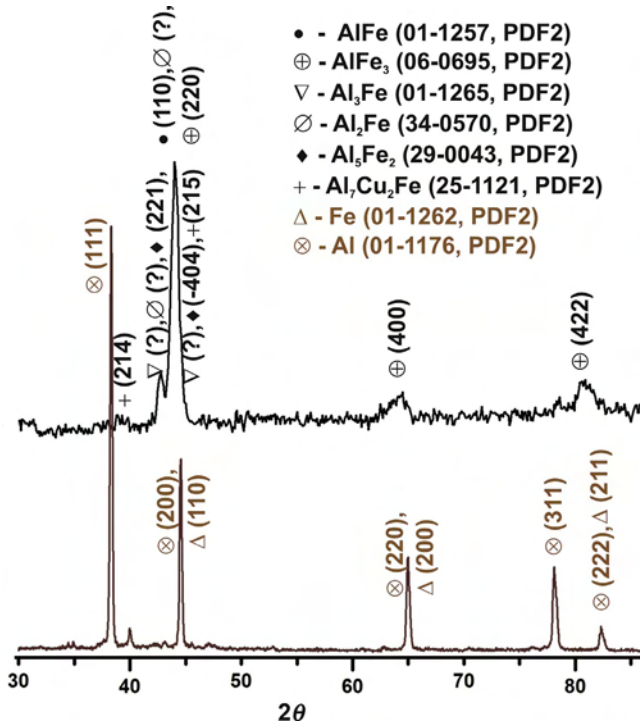


Figure 11.14 X-ray diffraction patterns of Fe-Al DMD multilayer system [22].

of the intermetallic compounds' synthesis. After the layered cladding, the strongest lines are located at the angles of $2\theta \sim 43\text{-}45^\circ$, which in our opinion, can correspond to the whole set of intermetallide phases. These can, disputably, be both the metastable phases, (222) Al₅Fe₂ and Al₂Fe, and stable phases, (110) AlFe and (220) AlFe₃. The existence of the AlFe₃ phase is confirmed by the presence of weaker reflexes (400) and (422) at larger angles.

The microelement analysis data (Figures 11.15 and 11.16) confirms our conclusions. A possibility of the presence of complex intermetallide compounds with a copper (215) Al₇Cu₂Fe should also be noted. This is connected with the copper presence in the initial composition of the Al alloy. So, on taking into account the entire set of peaks, it can be concluded that the lines system (Figure 11.15) best matches the line system of the Fe₃Al and FeAl intermetallic compounds.

Figures 11.15 and 11.16 show the greatly magnified SEM images of the same micro- and substructures, as before in Figure 11.12b and c, from the middle and top parts of the cladded layers. Figure 11.15a, in particular, corresponds to the structure section from Figures 11.12b1, Figure 11.15b from Figure 11.12b3, and Figure 11.16a-c from Figure 11.12c1-c3, respectively.

On the whole, their structures correspond to the above-given data of the optical metallography. However, the interesting results are those of element analysis. Relying on this data, we can assert that the preferred intermetallic yielding of FeAl crystals in

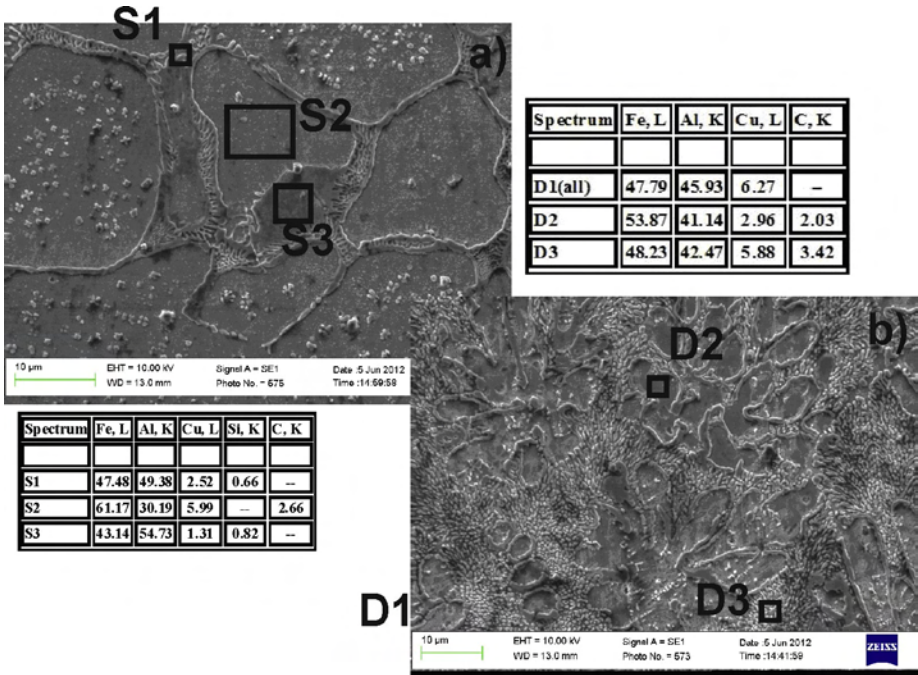


Figure 11.15 SEM micrographs showing typical solidification microstructures of middle clad coatings with EDS result of Fe-Al multilayer system [22].

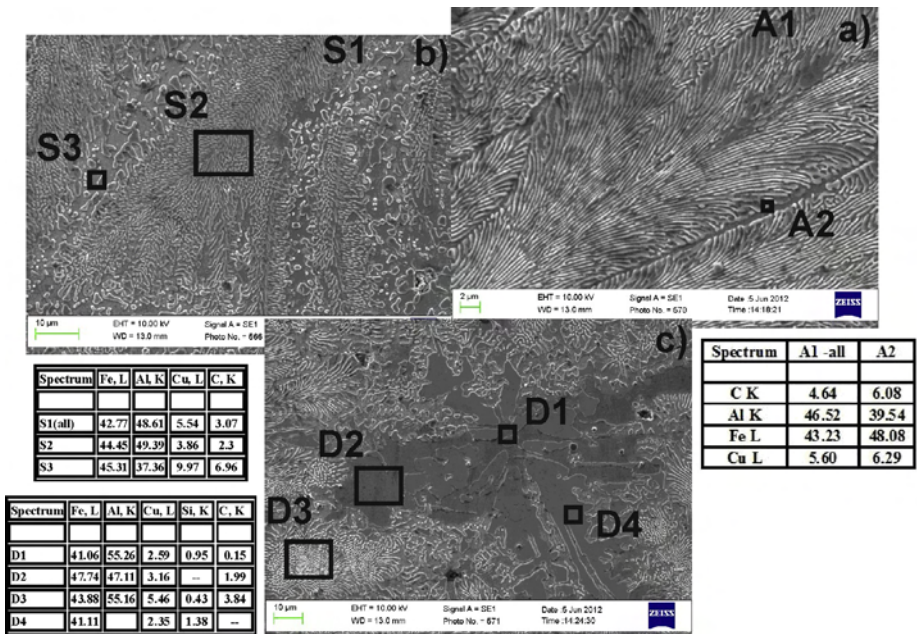


Figure 11.16 SEM micrographs showing typical solidification microstructures of top clad coatings with EDS results of Fe-Al multilayer system [22].

the middle layers from 4 to 6 mm and of the Fe_3Al phase in the layers from 2 to 4 mm take place, while in the top clad layers the phases of FeAl , FeAl_2 , Fe_2Al_5 are also generated.

Because hard but brittle FeAl_2 , Fe_2Al_5 intermetallide phases identified by the authors are the second phase inclusions for the iron clad matrix, they both strengthen this matrix and cause its cracking. An insignificant addition of Cu can smooth over this effect, however.

The element analysis also reveals the presence of carbon (up to 2-5%) and silicon (up to 1.5%), although there must be no trace of them in the initial mixture (see the XRD pattern results in [Figure 11.14](#)). Furthermore, in our opinion, the residual presence of oxygen is completely probable.

11.3.3 Laser synthesis in Ni-Al system

Superalloys based on nickel are widely used in high-temperature applications, as in turbine blades [52]. In this case, high-temperature oxidation is a problem.

The next powders were used for the FGS fabrication. The aluminium powder had 99 wt.% of Al (TLS Technik GmbH&Co.). The NiCr superalloy Diamalloy 1005 (Sulzer Metco Co.) was used as the Ni powder, which had the following chemical composition: Cr 21.5, Fe 2.5, Mo 9, Nb 3.7 wt.%, bal. Ni. The powder particles were mainly spherical, with 95% having the size of $\sim 80\text{-}100\ \mu\text{m}$. The steel substrates had a square shape with a width of 65 mm and a height of 5 mm. Diamalloy is equivalent to the Inconel 525 alloy, which was studied earlier in the DMD process [53]. It combines high strength, creep resistance, and stability to oxidation and corrosion; therefore, it is widely used in space, chemical, and naval applications. Therefore, the intermetallide phase's generation of a nickel aluminate into this superalloy matrix is an interesting task, substantially changing its mechanical properties. The FGS fabrication scheme in the Ni-Al system was shown above ([Figure 11.6](#)).

The optical metallography is presented in [Figure 11.17](#). As described earlier, the photographs are selected in order to show the characteristic microstructures based on the lower (a), middle (b-c), and upper (d) parts of the FGS after 3D laser cladding, that is, where the proportions of the powdered Ni + Al $\approx 3:1$; $1:1$, and $1:3$ by weight ratios were comprised. Under large magnification, these layers are presented on the inserts a1 for (a); b1 for (b); c1 and c2 for (c) and d1 for (d). In the lower layers in the photo ([Figure 11.17a and b](#)), a columnar dendrite pattern was observed that characterized the high-speed quenching of the NiCr superalloy, practically without Al additive participation [53]. The dendrite growth direction ([Figure 11.17a1 and b1](#)) is stipulated for maximum heat dissipation to the massive substrate. We connect superfluous porosity in [Figure 11.17a and b](#) (shown by arrows) with the nonoptimal selection of the increment height from one layer to the next. At the top layers ([Figure 11.17c and d](#)) the microstructure radically changes. In the middle (bottom of [Figure 11.17c](#) or c1), there is a cellular microstructure, which can testify to the equivalence of the heat dissipation speeds in different directions from this area. The upper layers ([Figure 11.17c2-d2](#)) have a needle-shaped microstructure with the impregnations of intermetallide phases. At the middle layers we also observed the triple eutectic structure, which consists of a γ -solid

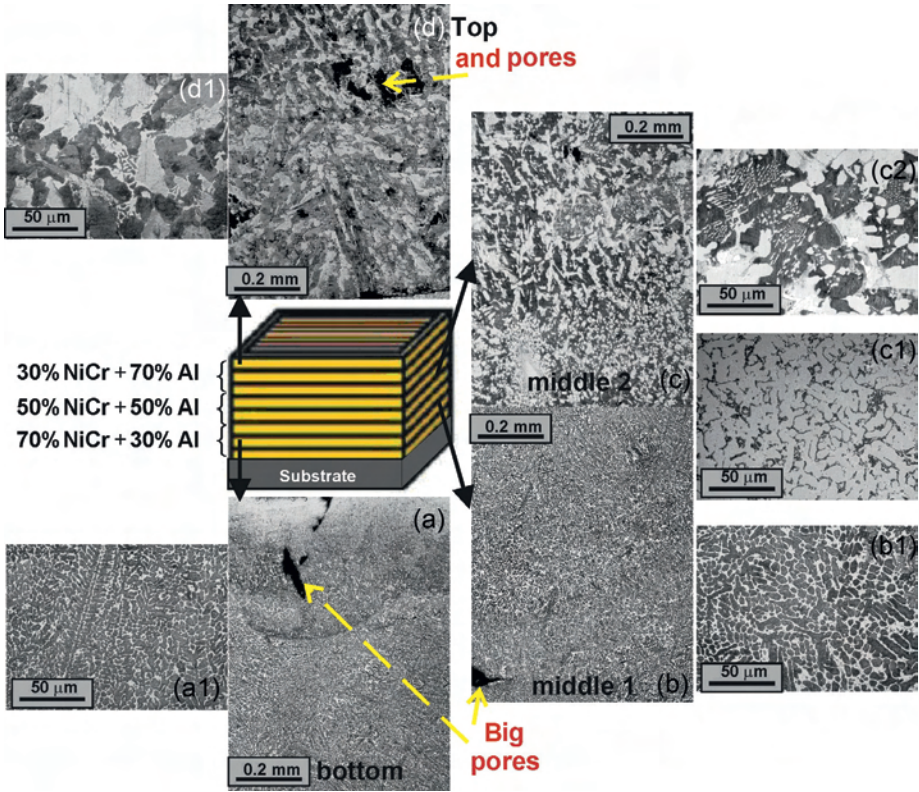


Figure 11.17 OM micrographs showing the typical microstructures of 3D laser clad coating of NiCr-Al multilayer system: (a) bottom layers $\sim 2\text{--}4$ mm from substrate; (b) middle layers $\sim 4\text{--}6$ mm from substrate; and (c) top layers $\sim 6\text{--}8$ mm from substrate.

solution on the nickel basis, α -solid solution on the chromium basis, and also β -solid solution on the basis of the Ni_3Al intermetallic compound in the middle and NiAl intermetallic phase above. By the boundaries of the $(\alpha + \gamma + \beta)$ triple eutectic colonies, the two-component eutectic is arranged, which includes the γ -solid solution on the Ni basis and AlCr_2 intermetallic phase.

The results of a microhardness measurement are shown in [Figure 11.18](#). If at near the base the microhardness is equal to $500\text{--}550 \text{HV}_{0.1}$, then it unevenly grows and reaches up to $650\text{--}750 \text{HV}_{0.1}$. The separate dips in the microhardness value we connect in the bottom layers (up to 2 mm from the substrate in [Figure 11.18](#)) with the superfluous porosity, and in the top layers with the indenter entry into the Diamalloy 1005 matrix. On the whole, the measured microhardness values considerably exceed other researchers' data ($500\text{--}550 \text{HV}_{0.1}$ for the LC of NiAl by Yu *et al.* [54]; $200\text{--}250 \text{HV}_{0.1}$ for the Inconel 625 after the DMD process by Dinda *et al.* [53]).

The XRD pattern of a transverse section after the LC in the NiCr-Al system is shown in [Figure 11.19](#). We can draw the following basic conclusions: After the LC free nickel and aluminium are practically absent, that is, it has completely interacted with the Ni_3Al and NiAl intermetallic phase formation. This distinguishes our results

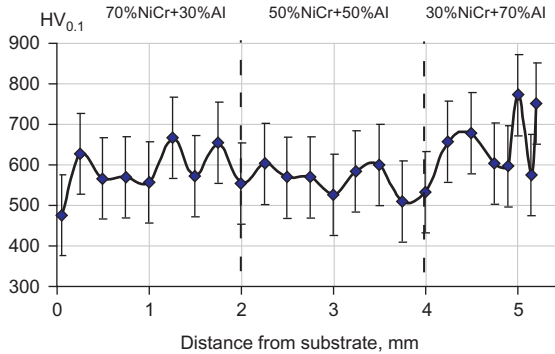


Figure 11.18 Microhardness distributions of NiCr-Al FG multilayer system.

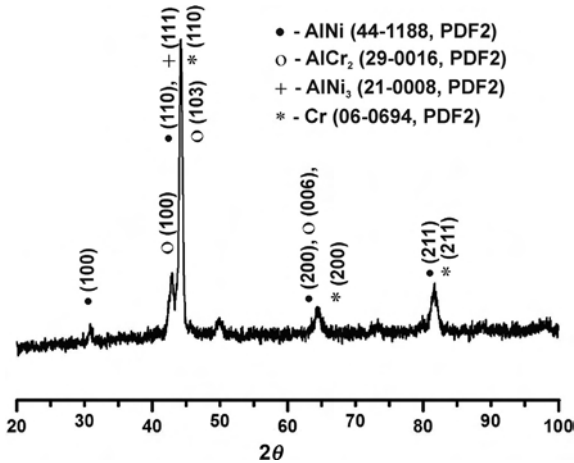


Figure 11.19 X-ray diffraction patterns of NiCr-Al DMD multilayer system.

from the data of the study in Ref. [53], which under similar LC regimes with the subsequent annealing fixed both the free nickel, γ - and δ -Ni₃Nb phases. Because the intensity lines of free chromium practically coincide with the intensity lines for the intermetallic compound AlNi, so it is impossible to assert unambiguously about the free Cr presence. Meanwhile, the presence of intermetallic phase of AlCr₂ is possible.

Figures 11.20 and 11.21 show the SEM data in the bottom, middle, and top layers of the FGS after the layerwise LC in the NiCr-Al system. The “All” index is written with those EDX data, in which information was collected from the whole area of the corresponding figure. Figure 11.20a completely coincides with the middle part of Figure 11.17a. It is evident that its microelement composition (S1-All) practically repeats the initial Diamalloy 1005 composition plus 10 wt.% of Al. Figure 11.20b corresponds to the lower part of Figure 11.17b, and Figure 11.20c to Figure 11.17b1. By the element relationship in the S2 area (Figure 11.20b) we have the Ni₃Al intermetallic phase, on the boundaries of which have been observed the free Cr extraction (see S3).

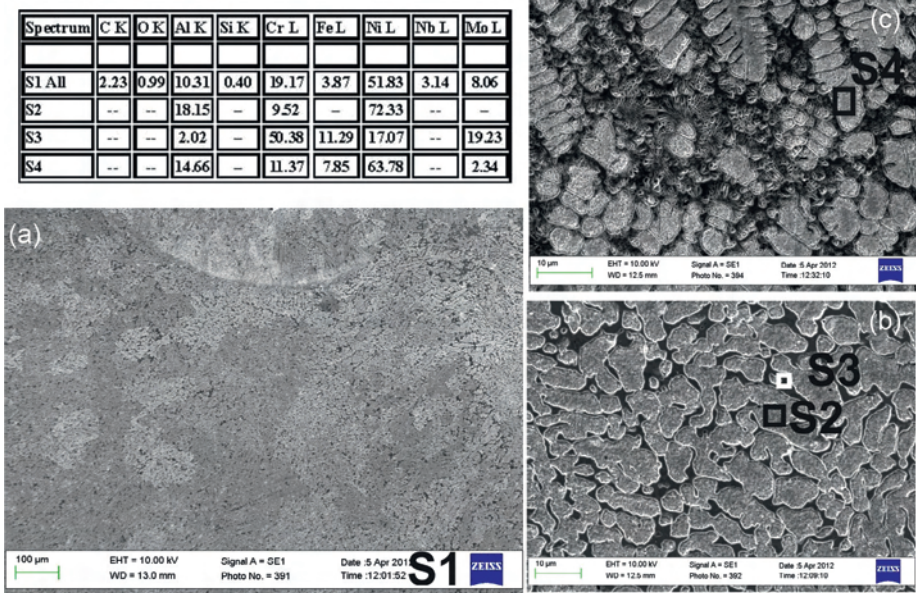


Figure 11.20 SEM micrographs showing typical solidification microstructures of the bottom (a, b) and middle (c) clad coatings with EDS result of NiCr-Al multilayer system.

Finally, a dendritic structure in [Figure 11.20c](#) (S4) clearly shows the intermetallide nature of the Ni_3Al phase. [Figure 11.21a](#) corresponds to [Figure 11.17c1](#), while [Figure 11.21b and c](#) is equivalent to [Figure 11.17c2](#) and [d1](#), respectively. We can assert that in the upper layers the synthesis of the NiAl intermetallide phases (D4 and D8) occurs; a precipitation of the AlCr_2 intermetallide phase on the grain boundaries (D2). We connect sufficiently great carbon (up to 10 wt.%) and oxygen (up to 6 wt.%) content with the possibility of their hit from the environment, although the XRD pattern does not fix these elements.

The applications of the 3D laser cladding for the creation of a functional gradient and building of Me_xAl_y ($x, y = 1, \dots, 3$) intermetallic structures has been experimentally studied. It has been shown that:

- the LAM process implementation has the tendency to form heterogeneous phases of Fe_3Al and FeAl. The microhardness growth from 300 to 900 HV was obtained for the same sample due to the change of the elements ratio in the Fe-Al system during the 3D laser cladding. The copper alloying additive is favorable for the smoothing of the crack tendency formation beyond to the intermetallic compound-steel matrix boundaries;
- the DMD process implementation in argon has the tendency to form the heterogeneous γ -phase of TiAl. Variations in microhardness from 130 to 800 HV have been obtained within the same sample due to the change of the element relationship in the Al-Ti system with 3D laser cladding;
- under the layerwise LC in the NiCr-Al system the formation of the Ni_3Al and NiAl intermetallic compounds was observed. The microhardness values from 500 to 750 $\text{HV}_{0.1}$ were achieved, which precisely connected with the intermetallide phase's presence in the NiCr matrix.

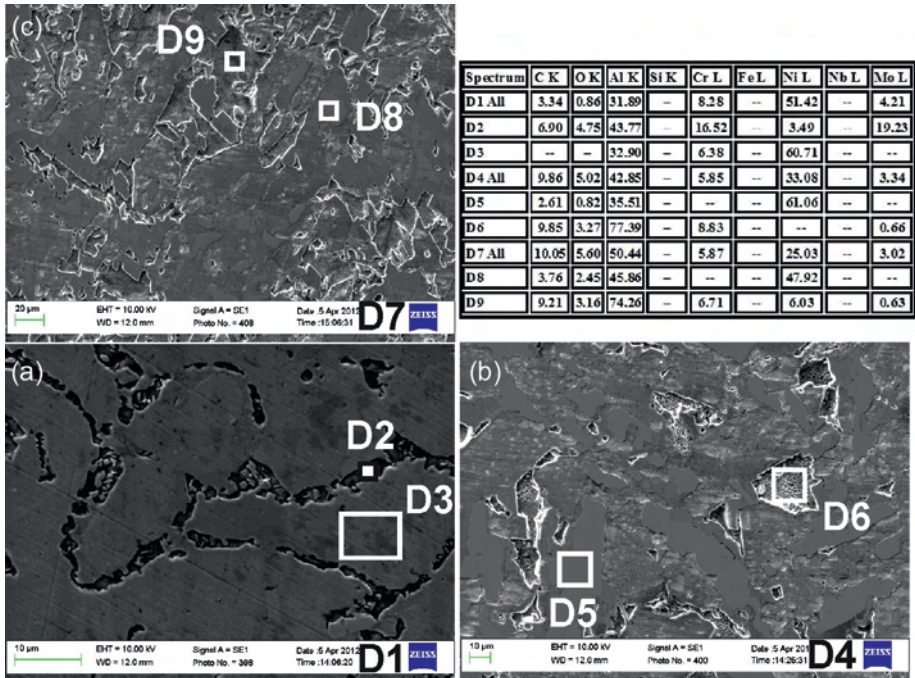


Figure 11.21 SEM micrographs showing typical solidification microstructures of the middle (a) and top (b, c) clad coatings with EDS results of NiCr-Al multilayer system.

It has been found that the sizes and boundaries of the transition zones between the powder compositions with different components and of corresponding Me_xAl_y intermetallic phases depend on the laser synthesis conditions and, thus, can be controllable.

The possibility of controlling the hardness of the multilayer structure by changing the powder composition and using the appropriate CAD modeling can expand the range of the 3D FGM applicability in the aerospace and nuclear industries. Provoking a further interest is the study of the LAM conditions for the large samples and the control of the residual stress level, which can impede the process application for the fabrication of high-precision samples.

11.4 Temperature distribution during the layerwise surface laser remelting of exothermal powder compositions

It is obvious that the determination of LI optimum regimes (power, scanning velocity, the beam diameter, etc.), which make it possible to realize the synthesis reaction of diffusion type for intermetallic compounds (i.e., controlled exactly in the laser beam spot), it is the urgent task both of SLS/M+SHS and LC+SHS processes in the Me + Al reactive powder compositions. The final goal of such a study is the layer-by-layer fabrication of the FG materials (3D parts) via the SLS/M or/and LC+SHS joint method,

using the feedback from the thermocouple measurements to control and guide the process.

A diagram of the setup for thermal measurements during the laser-controlled SHS-process is shown in [Figure 11.22](#) and was developed by Shishkovsky *et al.* [13,14]. Powder compositions were placed on a metal platform. The volume of cuvette was $\sim 12 \text{ cm}^3$. The dimensions of the LI zone were $10 \times 30 \text{ mm}^2$ with a typical sintered/melted monolayer depth of 0.5–3 mm. Thermocouples were inserted into the powder within this zone 5 mm from the zone edge at a depth of 3–5 mm.

[Figures 11.23–11.28](#) describe the character of temperature distribution in the reactive capable powder compositions, where SHS propagation waves can move in front of the laser beam. Regimes of the LI corresponded to the experimentally determined conditions for laser-controlled overlap of the SLS/M and SHS processes. As thermocouples were situated on the periphery of sintering/melting, absolute values of temperatures are not high. In the case of a thermal explosion, all the powder volume ($\sim 12 \text{ cm}^3$) was burned through completely; however, the contact points to the thermoelectric junction were not destroyed. This allowed us to register the temperature change over time for the whole process.

As a whole, the temperature profiles had an understandable sequence for all of the experiments ([Figures 11.23–11.28](#)).

The first response was always from the first thermocouple, which was positioned closest to the starting point for the initiation of the laser scanning. The second (counter) thermocouple, routinely behind the reaction front, does not record a temperature increase until some time later. Measurements from the third and fourth thermocouples are comparable with first one. It is connected as follows: when the reaction front reaches the midpoint of the sintered/melted monolayer ([Figure 11.22](#)), the powder volume is already very hot. If reaction control is lost, the temperature measurements for the third and fourth thermocouples are maximized. Finally, reaction exothermicity is

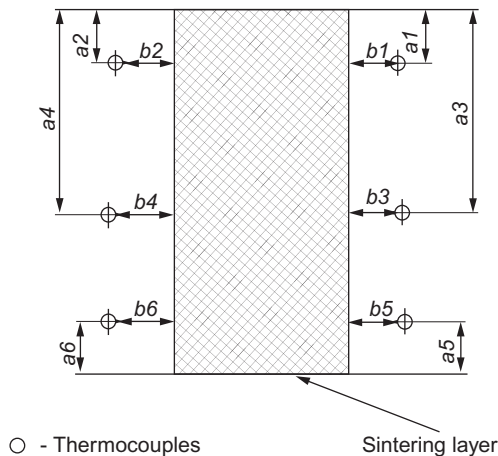


Figure 11.22 Scheme of thermocouples distribution ($i=1, \dots, 6$, a_i , b_i —sizes), relative the zone (hatching marked) of laser sintering/melting [13,14].

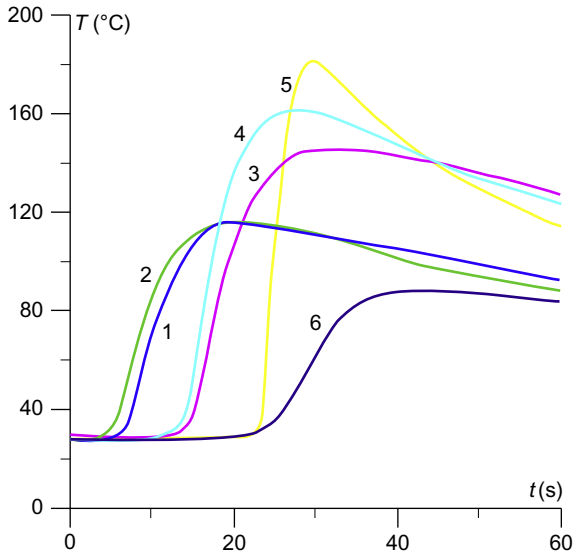


Figure 11.23 Temperature change on thermocouples ($i=1, \dots, 6$) during laser sintering/melting. Power composition Ni+Al=3:1. LI power $P=24$ W. Laser scan velocity $v=11.4$ cm/s, beam diameter $d=100$ μm [13,14].

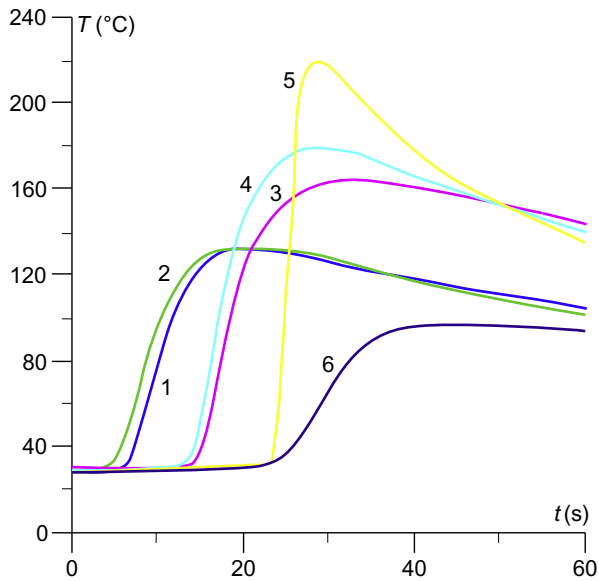


Figure 11.24 Temperature change on thermocouples ($i=1, \dots, 6$) during laser sintering/melting. Power composition Ni+Al=3:1. LI power $P=30.3$ W. Laser scan velocity $v=11.4$ cm/s, beam diameter $d=100$ μm [13,14].

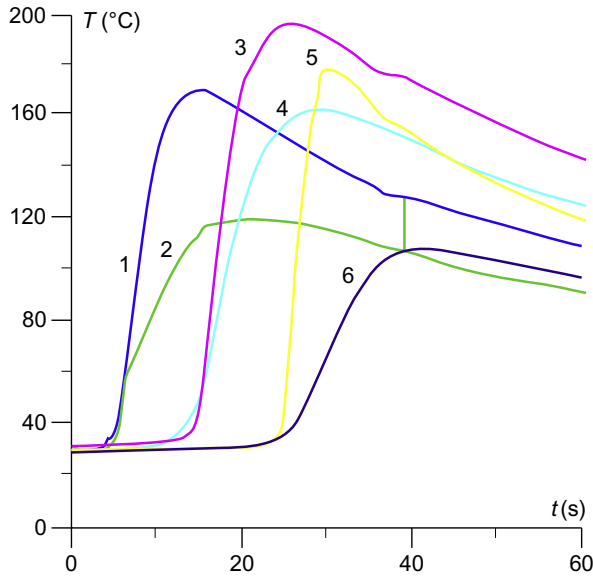


Figure 11.25 Temperature change on thermocouples ($i = 1, \dots, 6$) during laser sintering/melting. Power composition Ni+Ti = 1:1. LI power $P = 24$ W. Laser scan velocity $v = 11.4$ cm/s, beam diameter $d = 100 \mu\text{m}$ [13,14].

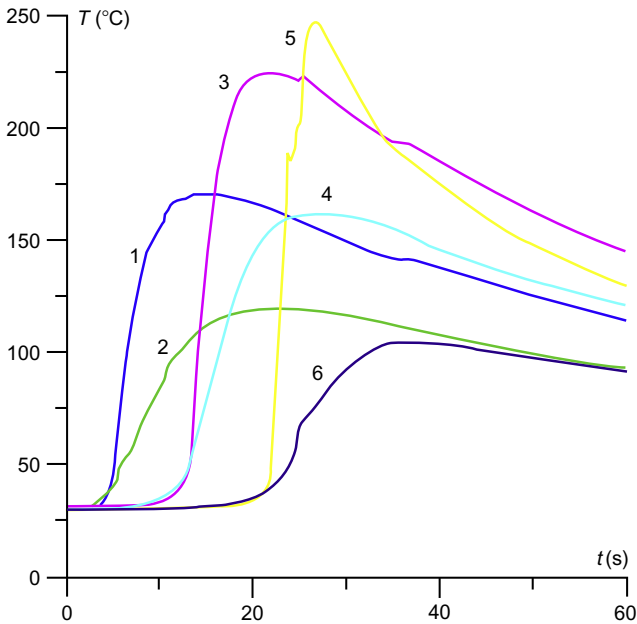


Figure 11.26 Temperature change on thermocouples ($i = 1, \dots, 6$) during laser sintering/melting. Power composition Ni+Ti = 1:1. LI power $P = 30.3$ W. Laser scan velocity $v = 11.4$ cm/s, beam diameter $d = 100 \mu\text{m}$ [13,14].

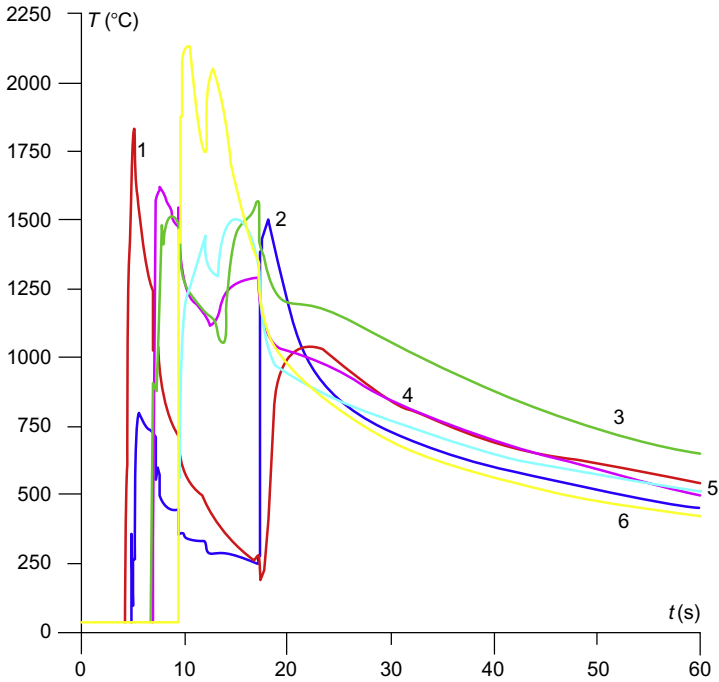


Figure 11.27 Laser sintering/melting of powder composition Ni+Al=1:1, beam diameter $d=100\ \mu\text{m}$. LI power $P=800\ \text{W}$, $v=11.4\ \text{cm/s}$ —pure nickel. Laser regime: $P=8\ \text{W}$, $v=11.4\ \text{cm/s}$ [13,14].

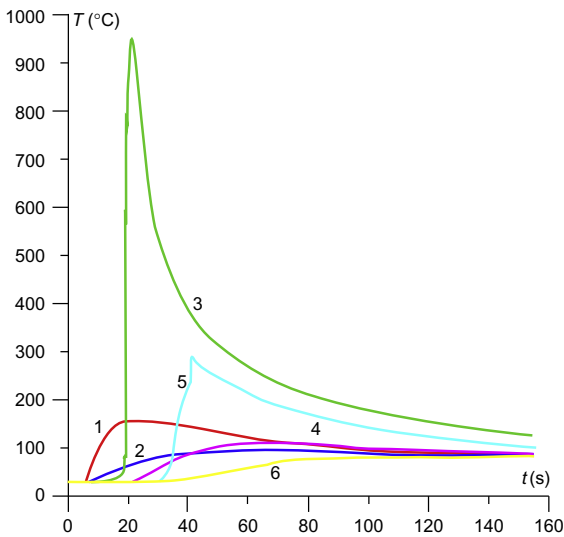


Figure 11.28 Laser sintering/melting of powder composition Ni+Al=1:1, beam diameter $d=100\ \mu\text{m}$. LI power $P=30.3\ \text{W}$, $v=2.9\ \text{cm/s}$ —PGSR4 nickel power. Laser regime: $P=8\ \text{W}$, $v=11.4\ \text{cm/s}$ [13,14].

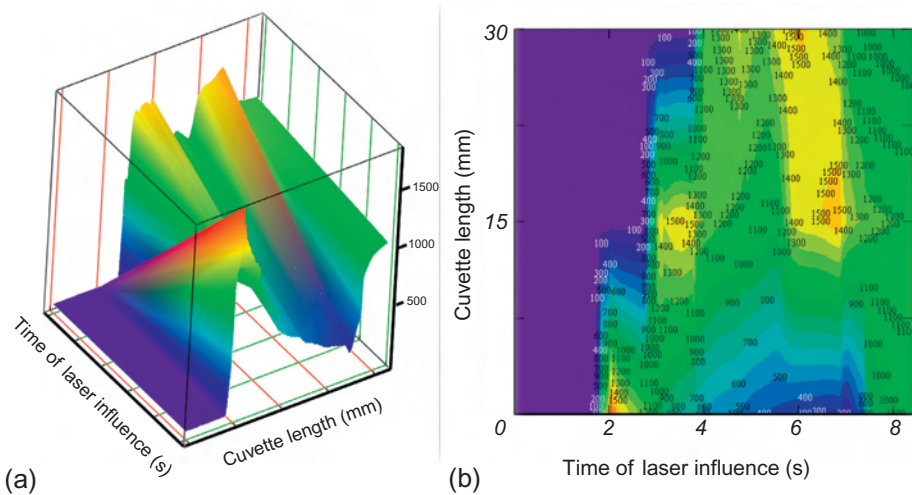


Figure 11.29 3D temperature field (a) and a front of exothermal reaction (b) relative to cuvette during LI.

registered from the fifth and sixth thermocouples, which are farther away from the initiation point.

Figure 11.29 shows the digitization results of the previously carried out measurements [13,14] of temperature distribution during the LI on the Ni+Al=1:1 powder composition with parameters that are the same as those in Figure 11.27. As is evident, there is a certain delay (~ 4 s) between the beginning of laser scanning by means of the powder surface and a real increase in the temperature. These measurements correlate with the calculations on the numerical model in Section 11.4 [23].

A two-dimensional transient theoretical model of the SLS/M and LC for the reactive powder compositions with allowance for chemical reaction kinetics has been developed in Section 11.5 [5]. The experimental data obtained in this study provides a good basis for comparing the numerical and experimental approaches.

11.5 Theoretical and numerical modelling of selective laser sintering/melting (SLS/M) and SHS hybrid processes

11.5.1 Theoretical modelling of the laser cladding and SHS processes overlapping

In this paragraph we will formulate base equations for the description of the layerwise remelting in reaction-capable powder composition on the substrate according to [55–66]. Because the 3D LC is a thermal process, the known equation of thermal conductivity plays a central role in the process of physical simulation. The equation of thermal conductivity (11.1) describes the energy balance in the selected volume: a

right side of equation includes diffusion and convection heat flows, taking into account all possible heat sources Q ; and left, a change in the heat quantity per unit of time and of volume. The system must be augmented by the momentum conservation and continuity equations (11.2). In the case of the thermomechanical process analysis, the connected system will consist of the thermal conductivity equations (11.1)–(11.4), plus equation of state (11.6), for the stresses and the strains. Note that Equation (11.6) becomes significant after the beginning of the crystallization process [67–69]. A scan velocity of the laser beam will designate V_L . It can be seen that an absorbed energy of the LI leads to the surface heating not more than the material boiling point T_B . Then, the heat losses can be seen to be due to the convection and thermal radiation in the comparison with the value of the absorbed power density Q .

$$\frac{\partial(\rho c T_L)}{\partial t} + \nabla(\rho c U T_L) = \nabla(\lambda \nabla T_L) + Q \quad (11.1)$$

Conservation equations are

$$\begin{aligned} \frac{\partial(\rho V_L)}{\partial t} + (\rho V_L \nabla) V_L &= \rho g - \nabla p + \mu \nabla(\nabla V_L) \\ \nabla V_L &= 0 \end{aligned} \quad (11.2)$$

where μ is the melting viscosity, g is the gravitational acceleration, and c , λ are the thermophysical parameters of the melting material. Under the reaction-capable powder cladding, the explicit form of Q includes the heat combustion due to the exothermic reaction. If a powder mixture is multicomponent, we will use an equation of type (11.22) for the thermophysical parameter description. Beyond the surface of the melt pool, the Marangoni force (11.3) acts [70,71], due to the inverse proportion of the surface tension from the temperature, and leading to the formation of the vortex flows in the melt from the center to the bath edges [72].

$$\begin{aligned} \nabla p + \rho g z &= \left(2\mu \frac{\partial V}{\partial n} n \right) + \gamma R \\ V n &= 0 \end{aligned} \quad (11.3)$$

where z is directed into the melt bath depth, γ is a surface tension, and R is a melt surface curvature. Under the surfactant species presence it is necessary to consider not only a temperature dependence of the surface tension coefficient, but the dependence of the chemical segregation concentration also:

$$\begin{aligned} \gamma(T, a_s) &= \gamma_0^m - A(T - T_0) - RT \Gamma_s \ln(1 + K_{\text{seg}} a_s) \\ \frac{\partial \gamma}{\partial T} &= -A - R \Gamma_s \ln(1 + K_{\text{seg}} a_s) - \frac{K_{\text{seg}} a_s}{1 + K_{\text{seg}} a_s} \frac{\Gamma_s \Delta H_0}{T} \end{aligned} \quad (11.3 \text{ a})$$

where $K_{\text{seg}} = S_1 \exp(-\Delta H_0/RT)$; ΔH_0 [J/mol] is the absorption heat, a_s [wt.%] is a concentration activity, S_1 a constant of the segregation entropy, and Γ_s [mol/m²] the

surplus outcome on the surface unit. This accounting can substantially change the traditional flow direction by Marangoni from the bath boundaries to the center [73].

On the liquid-solid boundary several conditions must also be carried out:

$$\begin{aligned}
 -\lambda_S \frac{\partial T_S(z=s(t)-0)}{\partial z} &= -\lambda_L \frac{\partial T_L(z=s(t)+0)}{\partial z} \pm \rho L \frac{\partial s}{\partial t} \left(1 + \left(\frac{\partial s}{\partial t} \right)^2 \right)^{-1} \\
 T_S(t, z=s(t, r), r) &= T_L(t, z=s(t, r), r) = T_m \\
 V_Z = V_R = V_\phi &= 0
 \end{aligned} \tag{11.4}$$

It is through these means that a convection current component on the “of solid-liquid” boundary tends to zero (known “adhesion condition”), the boundary temperature is equal to a crystallization temperature, and the crystallization front moves by law $s=s(t, R)$, a heat exchange and a latent heat output of phase transition occurs. The thermal equation for the crystallized phase, obviously, must also be mentioned here for system completeness.

An isotherm shape on the crystallization front ($T=T_{\text{Melt}}$)— $S(t, z, R)$ is found by the method of sequential approximations from the solution of a transcendental equation. For example, in the first approximation on the heating stage this dependence (11.5) can be presented as [71,74,75]

$$s(\zeta, 0) = s(t, 0) \frac{\zeta - t_L}{t - t_L}, \quad t_{LD} \leq t \tag{11.5}$$

where t_L, t_{LD} are the times of the melt appearance and the LI duration, respectively.

A visco-plastic (rheological) melt behavior after the crystallization acquires an elastic-plastic nature. Therefore, in the next elastic task in the cylindrical coordinate system it suffices to write

$$\begin{aligned}
 \frac{d\sigma_{rr}}{dr} + \frac{d\sigma_{rz}}{dz} + \frac{(\sigma_{rr} - \sigma_{\phi\phi})}{r} &= 0 \\
 \frac{d\sigma_{rz}}{dr} + \frac{d\sigma_{zz}}{dz} + \frac{\sigma_{rz}}{r} &= 0
 \end{aligned} \tag{11.6}$$

Equation (11.6) is supplemented to the Maxwell equation system, which connects the stresses, deformation, and displacement, taking into account a thermoelastic contribution up to plasticity; that is, on the free boundary (melt surface) an accepted definition is that the stresses are equal to zero. This system is solved, for example, by the thermoelastic potential method (Goodier’s function method) [67,69].

The LI source in the cylindrical coordinate system is described by Equations (11.17) and (11.18), and the boundary conditions take the form of type (11.23). On the remaining boundaries we will use equality conditions of zero temperatures in the semi-infinite thermal task. In the LC of finite quantity layers, the heat exchange according to the Newton law occurs (third order boundary conditions).

Thus, the closed theoretical model was built for the tasks of the laser synthesis of the 3D parts by the SLM/LC methods (analogy of the DMD™, LENS™, and 3D

Welding techniques). The above-formulated thermoelastic task could be solved by numerical methods. For example, in [58] this problem realizes in the ANSYS package, and in the FemLab program (Comsol Ltd.) was used. These solutions had been traditional for the laser surface hardening and alloying era of the 1980s, but contemporary software is now used, and it does not give answers on the some of the most important questions. Which will be the material structure after a high-speed crystallization? How will the AE be distributed, what phases will be obtained, and, as a result, what will the mechanical properties of the clad layers be? At the moment, these questions are solved by experimental methods. Meanwhile, in the following paragraph some model approaches will be presented, which enables us to answer some of these practical questions.

11.5.2 Kinetic and diffusion processes of high-speed crystallization under laser cladding and intermetallide alloying

Under the LC+SHS, overlapping the intermetallic compounds are synthesized into the melting bath. As a result of the high-speed quenching of the wide spectrum of the heterogeneous solid solutions with the intermetallic compounds, it is possible to obtain inclusions, which frequently do not correspond to the EPD for the studied system. Specifically, the possibility of retention in the solid lattice of the large intermetallide quantity due to the high cooling rates is the most interesting feature of the LC and MMC synthesis (see Section 11.2 regarding the FG layer's synthesis). The clad layer thickness can vary from 10 μm to several mm depending on the workable material and LI parameters. The structural phase state and their combination will determine the subsequent mechanical layer properties in many respects. These properties will also depend on the EPD of the corresponding compounds; a quantity of intermetallic phases; the degree of the mutual solubility (connectivity) between the matrix and intermetallic compound as the solid as liquid phases; the diffusion mobility of intermetallide phases on the phase boundaries (liquid-solid); the methods "transit" of these boundaries; the boundary moving speed during crystallization (i.e., from the cooling speed of the processed material); the ways of solid diffusion, and so on.

So the proposed theoretical model of the intermetallic compound redistribution under the LC could give the answers on these process directions and facilitate the optimization of the DMD regimes. It is obvious that because the material final state is most fundamental after the LC (this state is studied by experimental method now), the precisely high-speed crystallization of the melt with solid inclusions has great technological interest. It is assumed that intermetallic compound redistribution occurred already at the melt bath, but all insoluble phases for the LI time (particles of large sizes, compounds with high melting points, etc.) are incorporated at the solid phase directly in such a form as they existed before the fusion. Actually, already the first studies of the 3D LC showed [55,57,64] that the LI time ($\sim 0.1\text{-}1\ \mu\text{s}$) is sufficient for the effective mixing of the AE into the melt bath due to the existing of the convection currents there, which characterize the convection speeds up to $\sim 1\text{-}10\ \text{m/s}$.

The melt dynamic and the AE were analyzed earlier in sufficient details before the numerous studies (see for example [70,76–78] and the cited references).

The convective mixing task will not be examined in this study. Instead, a theoretical analysis of diffusion and kinetic redistribution of the AE on the final stage of the LC process will be presented. In particular, the processes on the crystallization front and in the cooling solid phase will be described.

We will assume from this point that the binary powder mixture is (Me + MeAl system), and the AE is an aluminide of the MeAl type (Me = Ni, Fe or Ti). It is reasonable to consider that the initial data is known: the temperature by the laser alloying zone on the moment of the LI finish $T(x_i, t)$ from the system solution (11.1)–(11.5); a quantity of synthesized intermetallide at the exothermic reaction $C_L = C_0 + C_{ad} + C_k$ (C_0 in accordance with the EPD); the Me_xAl_y metastable intermetallide phase quantity (if the same exist); and the EPD itself.

The process of high-speed crystallization of a melt and kinetics of a front moving during a phase transformation (PT) were also analyzed in the literature in detail (refer to monographs [79,80]). If the PT process of a first-order is interpreted classically, that is, it is realized by a way of thermofluctuational or atomic transitions on the boundary cross section of phases, so the growing velocity of the new phase (crystallized melt) is described as

$$\frac{\partial r}{\partial t} = av \exp\left(-\frac{U}{kT(t)}\right) \left[1 - \exp\left(-\frac{\Delta F}{kT(t)}\right)\right] \quad (11.7)$$

where v is the characteristic Debye frequency, U is the activation energy of the atom transition through the interphase boundary cross-section, ΔF is the changing of the specific free energy at the appearance the new phase nucleus (usually here it is limited by the volume part $\Delta F_v = \Delta h[T_m - T(t)]/T(t)$ and the surface part of $\Delta F_s = \phi\sigma n^{2/3}$ [81], and a is the lattice parameter. However, if the cooling velocity is very high, on the phase boundary the atoms begin to overcome cooperative [82] and fluctuation-diffusion nature of the transition loses meaning. In the work [81] from the analytical solution for the distribution function by particle number (DFPN) of the new phase $Z(n, t)$ it was shown that at the high-speed cooling, the melt is crystallized via clusters with the particle value from several tens to several hundred depending on a cooling velocity V_{cool} and material thermodynamic properties. At last, generally under $V_{cool} > V_{cr}$ the melting begins amorphously.

Further, we will use conclusions [81], in particular, for the lamellar (dendrite) shape embryos we found the exact form for the distribution function:

$$Z(\alpha, \beta, n) = \sqrt{\frac{n}{\alpha}} \int_0^\infty d\xi Z_{in}(\xi^2 e^\beta / 4) \exp\left(-\frac{4n + \xi^2}{4\alpha}\right) I_1\left(\xi \frac{\sqrt{n}}{\alpha}\right) \quad (11.8)$$

where Z_{in} is the initial distribution function, I_1 is a modified Bessel function of the first-order, T_0 is a temperature of phase transition, and α and β are the task parameters, which depend on the temperature changing rate $T(\tau)$:

$$\begin{aligned}\alpha(t) &= v \exp(-\beta(t)) \int_0^t \exp\left(\beta(\tau) - \frac{U}{kT(\tau)}\right) d\tau \\ \beta(t) &= -\frac{\Delta h v}{kT_0} \int_0^t \frac{T_0 - T(\tau)}{T(\tau)} \exp\left(-\frac{U}{kT(\tau)}\right) d\tau\end{aligned}\quad (11.9)$$

Then, the relative volume of the new crystallized phase can be defined as

$$\frac{\Delta V}{V} = 1 - \exp(\beta(t)) \quad (11.10)$$

and the average size of the crystalline nucleus or the average number of atoms in the nucleus of the new phase is defined as

$$\langle n \rangle = \frac{3\alpha(t)}{2} \left[\alpha(t) - 1 - \frac{1}{\alpha(t)} \ln \left(1 - \frac{\alpha(t)}{3} \right) \right] \quad (11.11)$$

In the paper [81], an asymptotic nature α and β under $t \rightarrow \infty$ was explored for the simplest cooling laws (linear, power, and exponential types) only. Here, we will consider that from the solution of the thermal conductivity Equations (11.1)–(11.5), the relative volume of a new phase, and the size of a crystallite we can estimate accurately through these parameters.

The knowledge of the temperature fields $T(t, z, R)$ in the liquid and solid phases, forms and speeds of the front displacement under the PT ($L \rightarrow S$) $S(t, z, r)$ from Equation (11.5), the volume and the size of the crystallizing phase (11.10) and (11.11) it allows us to mathematically adequately describe the diffusion redistribution process for the MeAl phase under the high-speed cooling from the melt pool during the LC process via an intermetallide alloying. The obtained Equation (11.10) in the physical sense is similar to a well-known Kolmogorov-Avrami equation for the new phase volume [79,80]. It should be considered that on the moving phase boundary the abrupt concentration changing for the AE takes place: $k_e = C_S/C_L$, where k_e is a ratio to a kinetic eutectic coefficient C_S (i.e., the AE concentration, determined by the solidus line on the EPD), and a C_L by the liquidus line [83,84]. Due to the closed equilibrium conditions, the equilibrium concentration of the dissolved atoms into the solid state cannot exceed the maximum solubility at the solid phase, therefore the maximum presence of the concentration admixtures after the LI testifies to the predominant role of the kinetic effects on the phase boundary (11.10) and (11.11). Phase reconstruction is accompanied by both the specific free energy decreasing $\Delta F_{(L \rightarrow S)}$ of the system and the latent heat output, but the atom volume is also decreasing in the concentration space [85]. This process differs from usual diffusion and is described by the specific set of equations [83,85]. For example, the Tiller model works for the very high speeds of the PT front motion, but works badly for low speeds. The Baker and Cahn model uses a thermodynamic approach, the Wood's model is based on the kinetic equations in the assumption of a very "thick" boundary zone, but the Jackson-Aziz model utilizes the kinetic laws. Without entering into the essence of these models, their basic conclusions could be pointed out. For the step-by-step movement of the PT front the

kinetic coefficient dependence of the motion speed for the $L \rightarrow S$ front could be presented as

$$k(v) = k_e + (1 - k_e) \exp\left(-\frac{v_D}{v}\right) \quad (11.12)$$

where $v_D = D_L/a$, D_L is the AE diffusion coefficient in the liquid phase. In the continuous front moving model ($L \rightarrow S$) this dependence is next:

$$k(v) = \frac{v/v_D + k_e}{v/v_D + 1} \quad (11.13)$$

In the Baker and Cahn model it is

$$k(v) = \frac{v/v_D + \ln(k_e)}{v/v + 1/k_e \ln(k_e) \exp(-v/v_D)} \quad (11.14)$$

The semi-infinite medium thermal problem has been described earlier (11.1)–(11.5). Let's designate the MeAl in a liquid phase $C_L(t, z, r)$ and in a solid phase $C_S(t, z, r)$. Let's assume that convection in the liquid phase is delayed on the distance l from interphase boundary $S(t, z, r)$ (i.e., l is interface thickness). Then at the boundary front speed $u = dS/dt$, the diffusion problem could be described

$$\begin{aligned} \frac{\partial C_{S,L}}{\partial t} &= D_{S,L}(T_{S,L}) \left(\frac{\partial^2 C_{S,L}}{\partial r^2} + \frac{1}{r} \frac{\partial C_{S,L}}{\partial r} + \frac{\partial^2 C_{S,L}}{\partial z^2} \right) + u \nabla C_{S,L} \\ 0 \leq r \rightarrow \infty, 0 \leq z \rightarrow \infty; C_L(t=0, r, z) &= C_L(t, z, r \in L) = C_L \\ C_S(t, r, z \rightarrow \infty) &= C_S \end{aligned} \quad (11.15)$$

$$\begin{aligned} -D_L(T_L) \frac{\partial C_L(z=s(t)-0)}{\partial z} &= -D_S(T_S) \frac{\partial C_S(z=s(t)+0)}{\partial z} \\ + \frac{\Delta V_{L \rightarrow S}}{V} (C_S(t) - C_L(t)) \frac{\partial s}{\partial t} & \end{aligned} \quad (11.16)$$

Equation (11.15) is described as the MeAl redistribution at the near-boundary region between the liquid and solid phases ($i = L, S$) and on the boundary itself (11.16). Moreover, the difference ($C_S - C_L$) on the PT front can be presented as $C_L[k(v) - 1]$, where $k(v)$ was determined before in (11.12)–(11.14). The concrete form of $k(v)$ selection makes it possible to realize different situations on the $L \rightarrow S$ front, when the interface (1) retains the AE in the melt and leads to their superfluous content on the surface, (2) forms the equilibrium redistribution, and (3) leads to the AE extraction at the second phase. The temperature dependence of the diffusion coefficient in the proper phase can be represented as $D_i = D_{i0} \exp(-E/kT_i(t, z, r))$.

The system solution can be achieved by numerical methods. Because the front moving speed will be known from the thermal conductivity equation solution (11.1)–(11.5), this facilitates the search for the system solution (11.12)–(11.16). One should consider that with the present definition the average AE concentration could be estimated in the solid phase. The metastable Me_xAl_y intermetallic redistribution requires the complication of system setting (11.12)–(11.16). As was noted earlier, the part of the intermetallic compounds cannot be dissolved completely for the LI time; however, in this case their sizes will decrease and some Al quantity will begin to precipitate in the melt. Undissolved intermetallic compounds will penetrate the phase boundary at the solid phase, to change the surface shape $S(t, z, R)$ and to create additional channels for the diffusion penetration of the MeAl from the liquid to the solid phase. A similar approach was examined at the [86]. Finally, if as a result of the high-speed cooling in the EPD some types of the intermetallic phases must be observed, and the system set (11.12)–(11.16) must be corrected.

Thus, the model approaches developed above, which include the kinetic and diffusion processes of high-speed crystallization after the LC, are completely closed. Actually, the above-mentioned continuous thermoplasticity task in connection with the AE redistribution under the cladding process can be solved by numerical methods only (ANSYS, Comsol packages). It allows us to give answers on the thermomechanical process's courses, and to facilitate the 3D LC+SHS regime optimization. The kinetic and diffusion laws' addition to this model approach during the high-speed crystallization (Section 11.5.2) completely locks our model. We can estimate the structurally sensitive parameters of the 3D LC technological process, that is, to predict before the experience: the material structure and the phase composition after the high-speed crystallization; the AE redistribution in the case of multicomponent powder compositions uses and the FG layer fabrication; and to forecast the future mechanical properties. At present, these questions are solved only by experimental methods.

11.5.3 Numerical simulation of laser-controlled heating of reaction-capable powdered compositions

In this paragraph we will use the earlier developed [23] two-dimensional model for the theoretical description of SLS/M of powder compositions in which the SHS reaction can be realized. It is necessary to note that, apart from the structural macrokinetics of the SHS processes, we have an interest not only in specifying the quasi-stationary model reaction regimes (their stability, self-propagation velocity, etc.) [87] but also in the conditions of keeping the process controllable due to the relevant modifications of the laser source parameters (power density Q_1 , velocity of laser scanning during SLS/M V_L , α is a volume absorption of the LI and the laser spot diameter— $d_L = 2r_n$). Laser power density will be determined as follows:

$$Q_1(t, x, z) = Q_m \exp\left(-\frac{(x - V_L t)^2}{r_n^2}\right) \exp(-\alpha z) \quad (11.17)$$

where Q_m is maximum density of the LI in the beam spot center:

$$Q_m = \frac{AxP}{\pi r_n^2} \quad (11.18)$$

It is important to understand how the laser scan velocity (V_L) will correlate with the moving velocity (U) of the combustion reaction front during the SLS/M (or LC)+SHS process's combination. The heat release due to the chemical transformations in the reacting mixture Q_2 will be described in accordance with the well-known macrokinetic approach [88], by the introduction of the dimensionless degree of transformation η , which accepts values from the segment $[0, 1]$ and satisfies (11.20), as

$$Q_2 = Q_R \rho \frac{\partial \eta}{\partial t} \quad (11.19)$$

$$\frac{\partial \eta}{\partial t} = F_\eta(\eta) k \exp\left(-\frac{E}{RT}\right) \quad (11.20)$$

Mathematically, the model can be formulated inside the two-dimensional half-space $(x, z) \in (-\infty, \infty) \times (0, \infty) = R \times R^+$. The positive direction of an O_x axis coincides with the direction of the laser beam movement, and the positive direction of the O_y axis is defined as going into the depth of the powder reaction mixture:

$$c\rho \frac{\partial T}{\partial t} = \lambda \left(\frac{\partial^2 T}{\partial x^2} + \frac{\partial^2 T}{\partial z^2} \right) + Q_1 + Q_2 \quad (11.21)$$

In order to simplify the formal part of the model, it is necessary to ensure that the density, heat capacity, and thermal conductivity of the reacting mixture do not change their values during the SLS/M process. For their values, the following approximation was utilized:

$$A = \frac{\rho}{v\rho_1 + (1-v)\rho_2} (vA_1 + (1-v)A_2) + \frac{v\rho_1 + (1-v)\rho_2 - \rho}{v\rho_1 + (1-v)\rho_2} A_a \quad (11.22)$$

where A_1, A_2, A_a are the heat capacity, thermal conductivity, and heat diffusivity of the initial components in air, v is the volume fraction of one component, and ρ is the bulk density of the reacting mixture. Initial and boundary conditions are as follows:

$$\left. \frac{\partial T}{\partial y} \right|_{y=0} = 0, \quad T(t, x = +\infty) = T_0, \quad \left. \frac{\partial T}{\partial x} \right|_{x \rightarrow \pm\infty} = 0 \quad (11.23)$$

$$T(0, x, y) = T_0, \quad \eta(0, x, y) = 0 \quad (11.23a)$$

We will connect the system of coordinates with the laser beam center by introducing a new variable parameter $z = x - V_L t$. Then combining (11.21), (11.17)–(11.20) will give

$$\begin{cases} c\rho \frac{\partial T}{\partial t} - c\rho V_L \frac{\partial T}{\partial x} = \lambda \left(\frac{\partial^2 T}{\partial x^2} + \frac{\partial^2 T}{\partial y^2} \right) + Q_m \exp \left(- \left(2 \frac{x}{d_L} \right)^2 \right) \exp \left(- \frac{y}{\alpha_L} \right) \\ + Q_R \rho \frac{\partial \eta}{\partial t} - Q_R \rho V_L \frac{\partial \eta}{\partial x} \\ \frac{\partial \eta}{\partial t} - V_L \frac{\partial \eta}{\partial x} = \frac{(1 - \eta) \exp \left(\frac{(T - T_R)}{\Delta_R T} \right)}{\Delta_t} \end{cases} \quad (11.24)$$

The equation set of (11.24) was solved by using different schemes, known as the alternating direction approach using the sweep method [23].

One of the main parts of the analysis of the proposed model is to examine the problem of interdependence between the laser scan speed and the thickness of the single layer in the completely reacted, chemically active powder mixture immediately behind the LI spot. From a practical point of view, it is of importance to calculate the single-layer thickness when carrying out SLS/M. First of all, it is necessary to note here two extreme scenarios.

Scenario 1. The velocity of SLS/M is very small. First, when the single layer of powder mixture is thin enough and/or with strong heat release from the system (for example, the powder mixture lays on a cool massive substrate). In this case the thermal wave of chemical transformation will be complicated and unstable. It will permanently overtake the SLS/M, but after a small period of time it will stop and wait for the SLS/M approach, because the wave is not capable of propagating by itself without external heating. Part of the reaction mixture transformation will take place in the front of the thermal wave, and the other part immediately in the SLS/M. The heat from the SLS/M, which will boost an already heated powder mixture, will overheat the reacting system, and, instead of sintering/melting of the reacting layer, combustion will take place. It will break the step-by-step scheme of structure formation by SLS/M. In this case, control is lost from the SLS/M process. Therefore, the extremely unfavorable conditions appearing during the product formation make this regime unacceptable for SLS/M technology.

For the second case of the low laser scan velocity, the other situation is relevant to a relatively thick layer of powder mixture. In this case, there is so much heat released during the SHS reaction that the SHS thermal transformation occurs. This kind of wave is well-known and investigated in the framework of SHS structural macrokinetics. The SLS/M here serves only as a thermal wave initiator and, after a short period of time, lags behind the synthesis wave. It is also a case of complete incompatibility of the combined SHS and SLS/M technologies, when process control by the use of SLS/M is completely lost. Such a regime may be qualitatively described within the framework of the model when a single layer with infinite width was described.

Scenario II. The high speed of the V_L . In this case, the SLS/M process also becomes uncontrollable due to the fact that even a thin layer of the green mixture has no time to react completely in the neighboring area before the laser spot is moved forward. This may lead to one of two possible situations. If the heat quantity in the system appears to be high enough for SHS reaction propagation in the absence of the SLS/M, the reaction again happens to be completely uncontrollable.

Alternatively, a fast green mixture will appear to be partially reacted. The suggested model allows an estimate of the geometrical characteristics and values of the laser scan velocity, which correspond to the formation of a single layer of completely reacted green mixture. This case takes place after a sufficient period of time from the zero point, in which the SLS/M started to move and has abandoned an observable neighboring area near the laser irradiation spot.

Figure 11.31 shows the numerical results for the LC of a reaction-capable Ni-Al powdered system. As can be seen from the comparisons, the favorable conditions of the intermetallide phase synthesis for the Ni_3Al and NiAl (Figure 11.31d and e) take place, and it is not favorable for the $NiAl_3$ phase synthesis. Comparison of the measured temperatures (Figures 11.24, 11.27, and 11.28) and calculated temperatures (Figures 11.30a, c and 11.31a-c) ensure that our numerical approach is efficient.

Thus, we presented the model, which makes it possible to estimate the correspondence between the geometric characteristics of the synthesized system and the LI parameter's values, under which the delivered layer completely reacts in the moving laser beam spot. The carried out calculations agree well with the experimental data [4,13,14,20], represented early in Section 11.3.

11.6 Conclusion

To summarise the results of this chapter, it is possible to assert that the laser-controlled synthesis of aluminides and regime optimization are solved for the Me + Al (Me = Ni, Fe, Ti) reaction-capable powder composition. The experimental results by the FGS fabrication in the MMC are discussed, where the intermetallic phases strengthened the metal matrix. The control capability by the mechanical properties (microhardness) within such FG clad layers was shown. The specific fractal features of self-organization in the synthesized substructures have been noted. The self-consistent model of the laser-controlled combination in the SLS/M + SHS and in LC + SHS processes is built. It allows for the indicated class of reaction-capable powder mixtures to calculate the optimum regimes for the LI, in the framework of which it is possible to realize the synthesis of the 3D samples. It was important to understand and to estimate that the laser scanning speed must be located in the dynamic equilibrium with the front speed of the exothermal reaction for the intermetallic phase synthesis. Simultaneously with this, the laser energy input must be sufficient for the effective aluminide synthesis, but it must not exceed the critical values (known as the thermal effects of the exothermic reaction) for each of the synthesized phases in SHS powder mixtures. Our numerical calculations confirm the observed experimental data.

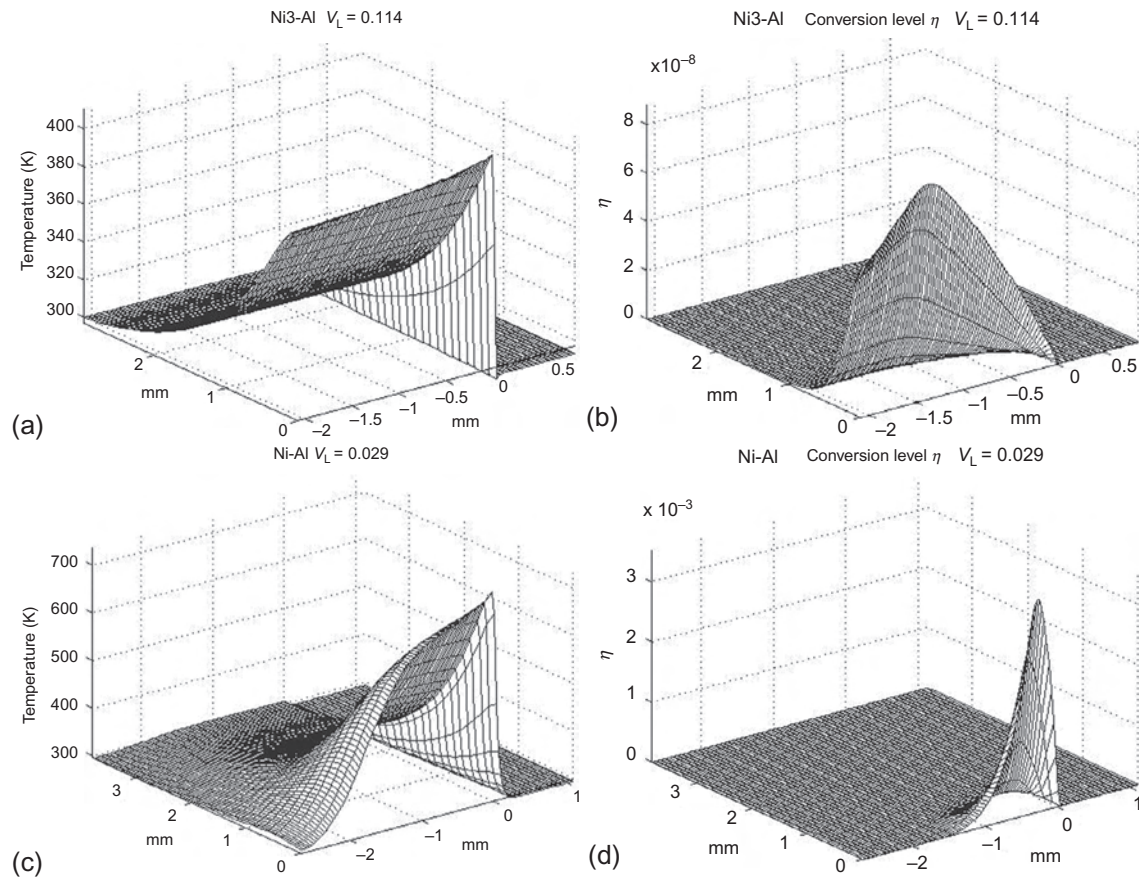


Figure 11.30 Temperature versus O_x and O_y axes (3D graph) (a, c) and conversion degree versus O_x and O_y axes (3D graph) (b, d). The case laser controlled SHS in Ni3-Al (a, b) system and Ni-Al (c, d) systems. The LI regimes were taken from [Figures 11.24](#) and [11.28](#), accordingly [23].

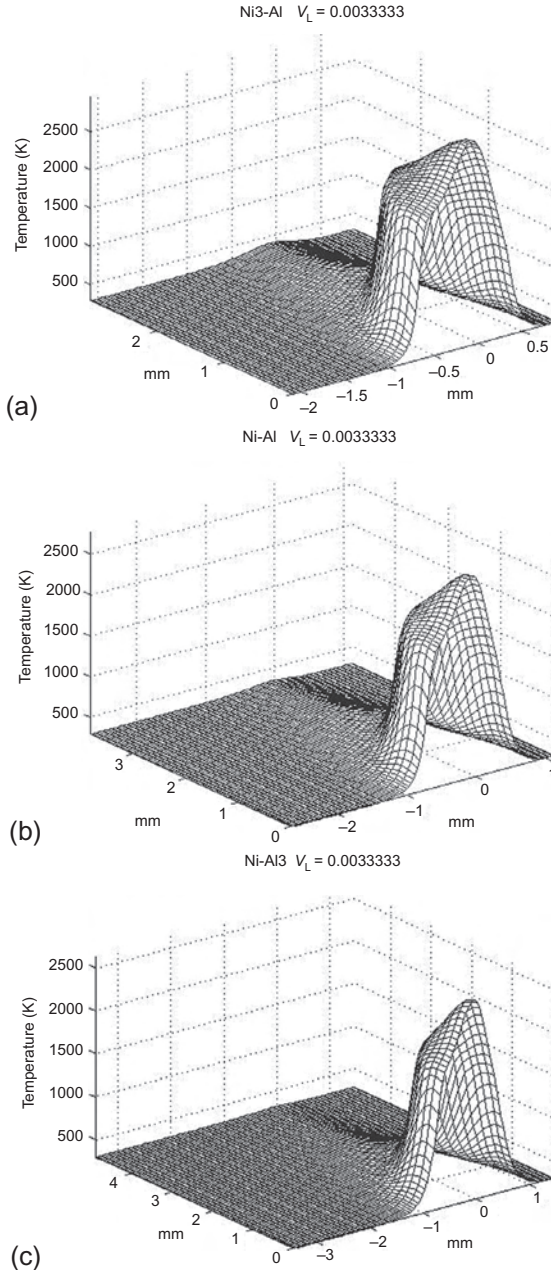


Figure 11.31 Temperature versus O_x and O_y axes (3D graph) (a-c) and conversion degree versus O_x and O_y axes (3D graph) (d-f). The case of LC+SHS overlapping in Ni3-Al (a, d) system, Ni-Al (b, e), and Ni-Al3 (c, f) systems. The LI regimes were taken from [Figure 11.27](#) [23].

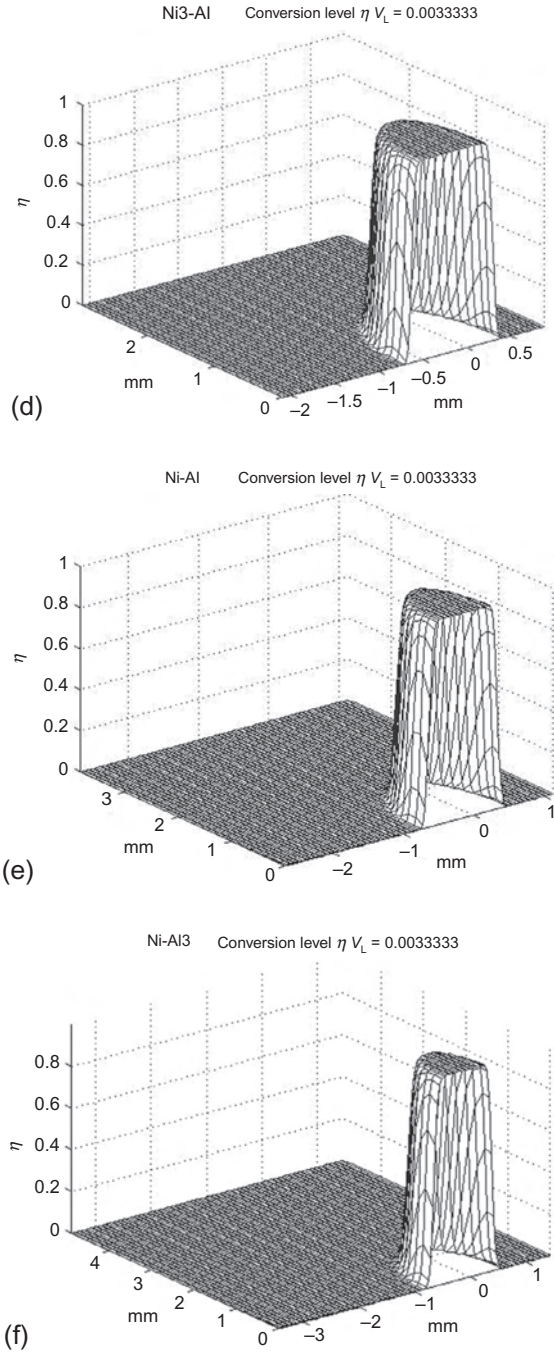


Figure 11.31 Continued.

Acknowledgment

This chapter was completed while the author was at Moscow State University of Technology “STANKIN” and was supported of the Ministry of Education and Science of Russian Federation in the frame of the Governmental Regulation of the Russian Federation N220 (contract No. 11. G34.31.0077). Separately, author thanks the Russian Science Foundation (grant N 14-19-00992) for continue of those studies (namely, Section 11.3 and numerical simulations mentioned in Sec. 11.5.3 – Figs. 11.31e–f).

References

- [1] I.V. Shishkovsky, *Laser Synthesis of Functional Mesostructures and 3D Parts*, Fizmatlit Publishers, Moscow, 2009.
- [2] D.K. Christoulis, M. Jeandin, E. Irissou, J.-G. Legoux, W. Knapp, Laser-assisted cold spray (LACS), in: D.C. Dumitras (Ed.), *Nd YAG Laser, InTech*, 2012. ISBN 978-953-51-0105-5.
- [3] H.Y. Lee, S.H. Jung, S.Y. Lee, K.H. Ko, Fabrication of cold sprayed Al-intermetallic compounds coatings by post annealing, *Mater. Sci. Eng. A* 433 (2006) 139–143.
- [4] I.V. Shishkovsky, A.G. Makarenko, A.L. Petrov, Conditions for SHS of intermetallic compounds with selective laser sintering of powdered compositions, *Combust. Explos. Shock Waves* 35 (2) (1999) 59–64.
- [5] L.P. Kholpanov, S.E. Zakiev, I.V. Shishkovskii, Modeling of thermal processes in laser sintering of reactive powder compositions, *J. Eng. Phys. Thermophys.* 78 (6) (2005) 1088–1095.
- [6] I.V. Shishkovsky, A.G. Makarenko, A.L. Petrov, Method manufacturing of 3D part from reaction-capable powder compositions, Patent Russian Federation No. 2217265, claim N 2000101975/02, 2000, date of priority 28.01.2000.
- [7] I.V. Shishkovsky, M.V. Kuznetsov, Y.G. Morozov, I.P. Parkin, Laser-induced SHS reactions and sintering of their products: computer-aided prototyping, *J. Mater. Chem.* 14 (2004) 3444–3448.
- [8] I.V. Shishkovskiy, M.V. Kuznetsov, Y. Morozov, I.P. Parkin, Electromotive force measurements in the combustion wave front during layer-by-layer surface laser sintering of exothermal powder compositions, *Phys. Chem. Chem. Phys.* 11 (2009) 3503–3508.
- [9] O.V. Lapshin, V.E. Ovcharenko, A mathematical model of high-temperature synthesis of nickel aluminide Ni_3Al by thermal shock of a powder mixture of pure elements, *Combust. Explos. Shock Waves* 32 (3) (1996) 299–305.
- [10] M.I. Shilyaev, V.E. Borzykh, A.R. Dorokhov, Laser ignition of nickel-aluminum powder system, *Combust. Explos. Shock Waves* 30 (2) (1994) 147–150.
- [11] I.V. Shishkovsky, I. Smurov, Y. Morozov, Nanofractal surface structure under laser sintering of titanium and nitinol for bone tissue engineering, *Appl. Surf. Sci.* 254 (4) (2007) 1145–1149.
- [12] A.V. Kamashev, A.S. Panin, et al., Laser-controlled synthesis of nickel-aluminum intermetallic compounds, *Tech. Phys. Lett.* 27 (2001) 498–499.
- [13] I.V. Shishkovsky, L.T. Volova, et al., Porous biocompatible implants and tissue scaffolds synthesized by selective laser sintering from Ti and NiTi, *J. Mater. Chem.* 18 (12) (2008) 1309–1317.
- [14] I.V. Shishkovsky, V.I. Scherbakov, et al., Surface laser sintering of exothermal powder compositions: the thermal and SEM/EDX study, *J. Therm. Anal. Calorim.* 91 (2) (2008) 427–436.

- [15] H.J. Glass, G. With, Fractal characterization of the compaction and sintering of ferrites, *Mater. Charact.* 47 (2001) 27–37.
- [16] I. Sinha, R.K. Mandal, Simulation studies on the nature of fractal dimensions of glass-ceramics at percolation threshold, *J. Mater. Sci.* 38 (2003) 3469–3472.
- [17] A. Provata, P. Falaras, A. Xagas, Fractal features of titanium oxide surfaces, *Chem. Phys. Lett.* 297 (1998) 484–490.
- [18] N. Bertolino, M. Monagheddu, et al., Ignition mechanism in combustion synthesis of Ti-Al and Ti-Ni systems, *Intermetallics* 11 (2003) 41–49.
- [19] S. Dadbakhsh, L. Hao, In situ formation of particle reinforced Al matrix composite by selective laser melting of Al/Fe₂O₃ powder mixture, *Adv. Eng. Mater.* 14 (2012) 45–48.
- [20] Y.G. Morozov, S.A. Nefedov, et al., Conditions of selective laser sintering in Al-Ti powdered system, *Izv. Akad. Nauk Ser. Fiz.* 66 (8) (2002) 1156–1159 (in Russian).
- [21] I. Shishkovsky, F. Missemmer, I. Smurov, Direct metal deposition of functional graded structures in Ti-Al system, *Phys. Procedia* 39 (2012) 382–391.
- [22] I. Shishkovsky, F. Missemmer, N. Kakovkina, I. Smurov, Intermetallics synthesis in the Fe-Al system via layer-by layer 3D laser cladding, *Crystals* 3 (2013) 517–529.
- [23] S.E. Zakiev, L.P. Kholpanov, et al., Modeling of the thermal processes that occur in the laser sintering of reacting powder compositions, *Appl. Phys. A Mater. Sci. Proc.* 84 (1–2) (2006) 123–129.
- [24] S. Ocylok, A. Weisheit, I. Kelbassa, Functionally graded multi-layers by laser cladding for increased wear and corrosion protection, *Phys. Procedia* 5 (2010) 359–367.
- [25] D. Srivastava, I.T.H. Chang, M.H. Loretto, The effect of process parameters and heat treatment on the microstructure of direct laser fabricated TiAl alloy samples, *Intermetallics* 9 (2001) 1003–1013.
- [26] W. Liu, J. DuPont, Fabrication of titanium aluminide matrix composites by laser engineered net shaping, in: *Proceedings of the Solid Freeform Fabrication Symposium*, Austin, TX, 2002, pp. 124–132.
- [27] N.V. Pimenova, T.L. Starr, Electrochemical and corrosion behavior of Ti-xAl-yFe alloys prepared by direct metal deposition method, *Electrochim. Acta* 51 (2006) 2042–2049.
- [28] S.C. Wei, B.S. Xu, et al., Comparison on corrosion-resistance performance of electrothermal explosion plasma spraying FeAl-based coatings, *Surf. Coat. Technol.* 201 (2007) 5294–5297.
- [29] Y. Yang, I. Baker, The influence of vacancy concentration on the mechanical behavior of Fe-40Al, *Intermetallics* 6 (1998) 167–175.
- [30] T.H. Kim, G.T. Gong, et al., Catalytic decomposition of sulfur trioxide on the binary metal oxide catalysts of Fe/Al and Fe/Ti, *Appl. Catal. Gen.* 305 (2006) 39–45.
- [31] C.T. Liu, E.P. George, et al., Recent advances in B2 iron aluminide alloys: deformation, fracture and alloy design, *Mater. Sci. Eng. A* 258 (1998) 84–98.
- [32] M.M. Pariona, V. Teleginski, et al., AFM study of the effects of laser surface remelting on the morphology of Al-Fe aerospace alloys, *Mater. Charact.* 74 (2012) 64–76.
- [33] T. Chmielewski, D.A. Golanski, New method of in-situ fabrication of protective coatings based on Fe-Al intermetallic compounds, *Proc. Inst. Mech. Eng. Part B J. Eng. Manuf.* 225 (2011) 611–616.
- [34] S. Kumar, V. Selvarajan, et al., Characterization and comparison between ball milled and plasma processed iron-aluminium thermal spray coatings, *Surf. Coat. Technol.* 201 (2006) 1267–1275.
- [35] G.J. Yang, H.T. Wang, et al., Effect of annealing on the microstructure and erosion performance of cold-sprayed FeAl intermetallic coatings, *Surf. Coat. Technol.* 205 (2011) 5502–5509.

- [36] S. Azem, M. Nechiche, K. Taibi, Development of copper matrix composite reinforced with FeAl particles produced by combustion synthesis, *Powder Technol.* 208 (2011) 515–520.
- [37] E. Godlewska, S. Szczepanik, et al., FeAl materials from intermetallic powders, *Intermetallics* 11 (2003) 307–312.
- [38] A. Agarwal, Iron aluminide based coating deposited by high energy density processes, *Surf. Modificat. Technol.* XV (2002) 173–182.
- [39] G. Sharma, R. Awasthi, K. Chandra, A facile route to produce Fe-Al intermetallic coatings by laser surface alloying, *Intermetallics* 18 (2010) 2124–2127.
- [40] B. Song, S. Dong, et al., Fabrication and microstructure characterization of selective laser-melted FeAl intermetallic parts, *Surf. Coat. Technol.* 206 (2012) 4704–4709.
- [41] S. Tomida, K. Nakata, Fe-Al composite layers on aluminum alloy formed by laser surface alloying with iron powder, *Surf. Coat. Technol.* 174 (2003) 559–563.
- [42] K. Uenishi, Y. Ogata, et al., Laser cladding of Fe-Cu based alloys on aluminum, *Solid State Phenom.* 127 (2007) 331–336.
- [43] L. Zhao, M.J. Zhao, et al., Study on Fe-Al-Si in situ composite coating fabricated by laser cladding, *Appl. Surf. Sci.* 258 (2012) 3368–3372.
- [44] L.N. Zhu, B.S. Xu, et al., Microstructure and nanoindentation measurement of residual stress in Fe-based coating by laser cladding, *J. Mater. Sci.* 47 (2012) 2122–2126.
- [45] S. Nayak, L. Riester, et al., Micromechanical properties of a laser-induced iron oxide-aluminum matrix composite coating, *J. Mater. Res.* 18 (2003) 833–839.
- [46] S. Chen, J. Huang, et al., Influence of a Ni-foil interlayer on Fe/Al dissimilar joint by laser penetration welding, *Mater. Lett.* 79 (2012) 296–299.
- [47] H. Laukant, C. Wallmann, et al., Fluxless laser beam joining of aluminium with zinc coated steel, *Sci. Technol. Weld. Joining* 10 (2005) 219–226.
- [48] S. Mukherjee, S. Chakraborty, Transport phenomena in conduction mode laser beam welding of Fe-Al dissimilar couple with Ta diffusion barrier, *Int. J. Heat Mass Transfer* 53 (2010) 5274–5282.
- [49] K. Saida, W. Song, K. Nishimoto, Diode laser brazing of aluminium alloy to steels with aluminium filler metal, *Sci. Technol. Weld. Joining* 10 (2005) 227–235.
- [50] G. Sierra, P. Peyre, Steel to aluminium braze welding by laser process with Al-12Si filler wire, *Sci. Technol. Weld. Joining* 13 (2008) 430–437.
- [51] M. Potesser, T. Schoeber, et al., The characterization of the intermetallic Fe-Al layer of steel-aluminum weldings, in: S.M. Howard, R.L. Stephens, C.J. Newman, J.-Y.J. Hwang, A.M. Gokhale, T.T. Chen (Eds.), *EPD Congress 2006*, TMS (The Minerals, Metals & Materials Society), 2006, pp. 167–176.
- [52] R. Vilar, E.C. Santos, P.N. Ferreira, et al., Structure of NiCrAlY coatings deposited on single-crystal alloy turbine blade material by laser cladding, *Acta Mater.* 57 (18) (2009) 5292–5302.
- [53] G.P. Dinda, A.K. Dasgupta, J. Mazumder, Laser aided direct metal deposition of Inconel 625 superalloy: microstructural evolution and thermal stability, *Mater. Sci. Eng. A* 509 (2009) 98–104.
- [54] Y. Yu, J. Zhou, J. Jianmin Chen, et al., Preparation, microstructure and tribological behavior of laser cladding NiAl intermetallic compound coatings, *Wear* 274–275 (2012) 298–305.
- [55] J. Choi, L. Han, Y. Hua, Modeling and experiments of laser cladding with droplet injection, *J. Heat Transfer* 127 (9) (2005) 978–986.
- [56] R. Dwivedi, S. Zekovic, R. Kovacevic, A novel approach to fabricate uni-directional and branching slender structures using laser-based direct metal deposition, *Int. J. Mach. Tools Manuf.* 47 (2007) 1246–1256.

- [57] S. Ghosh, J. Choi, Modeling and experimental verification of transient/residual stresses and microstructure formation of multi-layer laser aided DMD process, *J. Heat Transfer* 128 (7) (2006) 662–679.
- [58] M. Labudovic, D. Hu, R. Kovacevic, A three dimensional model for direct laser metal powder deposition and rapid prototyping, *J. Mater. Sci.* 38 (2003) 35–49.
- [59] M.P. Mughal, H. Fawad, et al., Deformation modelling in layered manufacturing of metallic parts using gas metal arc welding: effect of process parameters, *Model. Simul. Mater. Sci. Eng.* 13 (7) (2005) 1187–1204.
- [60] M.P. Mughal, H. Fawad, R. Mufti, Finite element prediction of thermal stresses and deformations in layered manufacturing of metallic parts, *Acta Mech.* 183 (1–2) (2006) 61–79.
- [61] M.P. Mughal, H. Fawad, R. Mufti, Three-dimensional finite-element modelling of deformation in weld-based rapid prototyping, *Proc. Inst. Mech. Eng. Part C J. Mech. Eng. Sci.* 220 (6) (2006) 875–885.
- [62] A.J. Pinkerton, L. Li, An analytical model of energy distribution in laser direct metal deposition, *Proc. Inst. Mech. Eng. Part B J. Eng. Manuf.* 218 (4) (2004) 363–374.
- [63] A.J. Pinkerton, L. Li, The development of temperature fields and powder flow during laser direct metal deposition wall growth, *Proc. Inst. Mech. Eng. Part C J. Mech. Eng. Sci.* 218 (5) (2004) 531–542.
- [64] A.J. Pinkerton, L. Li, An experimental and numerical study of the influence of diode laser beam shape on thin wall direct metal deposition, *J. Laser Appl.* 17 (1) (2005) 47–56.
- [65] H. Qi, J. Mazumder, H. Ki, Numerical simulation of heat transfer and fluid flow in coaxial laser cladding process for direct metal deposition, *J. Appl. Phys.* 100 (2006) 2.
- [66] E. Toyserkani, A. Khajepour, S. Corbin, *Laser Cladding*, CRS Press, 2005.
- [67] I.V. Shishkovskii, Calculation of residual stresses induced during laser quench-hardening of steel, *J. Eng. Phys. Thermophys.* 61 (6) (1991) 1534–1541.
- [68] I.V. Shishkovsky, Thermal field analysis under SLS of metal-polymer powder compositions, *Proc. SPIE* 4644 (2002) 446–449.
- [69] I.N. Zavestovskaja, V.I. Igoshin, et al., Theoretical and numerical analysis of stresses in a laser hardening model, *J. Sov. Laser Res.* 12 (4) (1991) 365–382.
- [70] N.N. Rukalin, *Laser and e-Beam Treatment of Materials*, Handbook, Mashinistrienie Publishers, Moscow, 1986 (in Russian).
- [71] A.A. Vedenov, G.G. Gladush, *Physical Processes of Laser Treatment of Materials*, Energoatomizdat Publishers, Moscow, 1985 (in Russian).
- [72] L.D. Landau, E.M. Lifshitz, Fluid mechanics, in: *Course of Theoretical Physics*, vol. 6, second ed., Reed Educational and Professional Publishing Limited, 2000.
- [73] G. Ehlen, A. Ludwig, P.R. Sahm, Simulation of time-dependent pool shape during laser spot welding: transient effects, *Metall. Mater. Trans. A* 34A (2003) 2947–2961.
- [74] A.A. Uglov, O.G. Sagetdinov, Melt simulation and metal crystallization under impulse laser, *Phys. Chem. Mater. Treat.* 5 (1991) 36–40 (in Russian).
- [75] A.A. Uglov, O.G. Sagetdinov, Melt simulation under volume laser influence, *Phys. Chem. Mater. Treat.* 5 (1992) 33–37 (in Russian).
- [76] T.K. Anthony, H.E. Cline, Surface rippling induced by surface-tension gradient during laser surface melting and alloying, *J. Appl. Phys.* 48 (9) (1977) 3888–3894.
- [77] R.V. Arutynov, V.I. Baranov, et al., *Interaction of Laser Influence with Matter*, Science Publishers, Moscow, 1989 (in Russian).
- [78] T. Change, J. Mazumder, Two-dimensional transient model for mass transport in laser surface alloying, *J. Appl. Phys.* 57 (6) (1985) 2226–2232.
- [79] J. Christian, *Theory of Transformation in Metals and Alloys*. Part 1, World Publishers, Moscow, 1987.

-
- [80] B.Y. Lubov, Theory of Crystallization in large Volumes, Science Publishers, Moscow, 1975.
- [81] I. Shishkovsky, Submicron nucleation kinetics during a high-speed laser assisted surface modification, *Phys. Status Solidi A* 207 (5) (2010) 1154–1159.
- [82] D.M. Gureev, S.I. Mednikov, About of theory of lattice reconstruction under phase transformations in metals, in: *FIAN Proceedings, 2017, 1993*, pp. 37–41 (in Russian).
- [83] M.J. Aziz, Model for solute redistribution during rapid solidification, *J. Appl. Phys.* 53 (2) (1982) 1158–1168.
- [84] M.J. Aziz, Non-equilibrium interface kinetics during rapid solidification: theory and experiment, *Mater. Sci. Eng.* 98 (1988) 369–372.
- [85] Pout, et al., Modification and Alloying of Surface under Laser, Ion and e-Beam Influence, Mashonostroenie Publishers, Moscow, 1987 (in Russian).
- [86] R. Sasikumar, T.R. Ramamohan, B.C. Pai, Critical velocities for particle pushing by moving solidification fronts, *Acta Metall.* 37 (7) (1989) 2085–2091.
- [87] S.E. Zakiev, K.G. Shkadinsky, Thermal influence of high frequency radiation on high-temperature synthesis front, *Chem. Phys. Rep.* 17 (1998) 112–120.
- [88] A.G. Merzhanov, History and new developments in SHS, *Ceram. Trans.* 56 (1995) 3–25.
- [89] K.J. Lee, S. Kumai, T. Arai, Interfacial microstructure and strength of steel to aluminum alloy lap joints welded by a defocused laser beam, *Mater. Trans.* 46 (2005) 1847–1856.
- [90] I.V. Shishkovskij, Fractal dimension of the pores distribution under a laser sintering of Ti powder, *Phys. Chem. Mater. Treat.* 6 (2004) 66–70 (in Russian).
- [91] I.V. Shishkovsky, I. Smurov, Titanium base functional graded coating via 3D laser cladding, *Mater. Lett.* 73 (2012) 32–35.